Research Square

Preprints are preliminary reports that have not undergone peer review.
They should not be considered conclusive, used to inform clinical practice,
or referenced by the media as validated information.

Fractionation of trace elements and sulfur isotopes during fluid evolution in the Darasun goldfield

Valeriya Brovchenko

valeriiabrovchenko@gmail.com

Institute of Geology of Ore Deposits Petrography Mineralogy and Geochemistry

Vsevolod Prokofiev

Institute of Geology of Ore Deposits Petrography Mineralogy and Geochemistry

Vera Abramova

Institute of Geology of Ore Deposits Petrography Mineralogy and Geochemistry

Sofia Selektor

Frumkin Institute of Physical Chemistry and Electrochemistry Russian Academy of Sciences

Ilya Vikentiev

Institute of Geology of Ore Deposits Petrography Mineralogy and Geochemistry

Research Article

Keywords: sulfides, magmatic-hydrothermal deposit, gold deposit, Darasun, sulfur isotopes, LA-ICP-MS

Posted Date: November 4th, 2026

DOI: https://doi.org/10.21203/rs.3.rs-11433371/v1

License: This work is licensed under a Creative Commons Attribution 4.0 International License.
Read Full License

Additional Declarations: No competing interests reported.

Fractionation of trace elements and sulfur isotopes during fluid evolution in the Darasun goldfield

Valeriya Brovchenko[1*], Vsevolod Prokofiev[1], Vera Abramova[1], Sofia Selektor[2], Ilya Vikentiev[1]

[1]*Institute of the Geology of Ore Deposits, Petrography, Mineralogy, and Geochemistry (IGEM), Russian Academy of Sciences, 109017 Moscow, Russia*

[2] *A.N. Frumkin Institute of Physical Chemistry and Electrochemistry RAS, 119071, Moscow, Russia*

*Corresponding author: Valeriya Brovchenko valeriiabrovchenko@gmail.com

Abstract

The Darasun goldfield in the Eastern Transbaikalia comprises three gold deposits, Talatui, Teremkyn and Darasun, considered to represent progressively periphery parts of an intrusion-related hydrothermal system with porphyry-style features. The trace element and sulfur isotope ($\delta^{34}S$) compositions of pyrite, chalcopyrite, arsenopyrite, galena, sulfosalts, and sphalerite were investigated using electron probe microanalysis (EPMA), laser ablation inductively coupled plasma mass spectrometry (LA-ICP-MS), and both in situ and bulk sulfur isotope analyses. Cooling and fractionation away from the granitoid intrusion are expressed by systematic decrease in Co, W, and Co/Ni and increase in Sb, Sn, and Au in sulfides. The concentrations of mineral-controlled elements in pyrite show systematic but non-monotonic variations from close-to-source Talatui to outlying Darasun deposit. Copper, Zn, In, and Ag contents in pyrite increase towards the periphery, whereas Ga, Se, Cd, and Te decrease, with pronounced depletion at the Teremkyn, reflecting change in sulfide assemblages and fluid evolution. At the Darasun deposit, three pyrite generations are identified. Pyrite 1 preserves an early, high-temperature signatures comparable to that of close-to-source Talatui. Pyrite 2 represents the main sulfide-forming stage and contains abundant sphalerite and sulfosalts inclusions, together with the highest As/Co ratio, and contents of Au and As. Fine-grained Py3 is enriched in Zn, In, Pb, Bi, Ag, Sn, and Tl, with Zn and In exceeding those of coexisting chalcopyrite, consistent with late reworking of earlier Py2. Based on our new and published data, $\delta^{34}S$ values of sulfides from all three deposits are near-magmatic and become lighter from Talatui (median 0‰) to Teremkyn (–1.1‰), and Darasun (–1.0‰), which is consistent with cooling and increasing isotope fractionation from homogeneous magmatic fluid. The Darasun deposit sulfides show a bimodal distribution with modes at –1.5‰ and +0.8‰. The dominant negative population formed from a reduced magmatic-hydrothermal fluid with $\delta^{34}S_{\Sigma S} \approx 0$‰, whereas the subordinate positive population is confined to veins close to anhydrite-bearing domains, requiring localized interaction between the reduced fluid and an isotopically heavy sulfate reservoir. These results show that preexisting sulfates can supply heavy sulfur to later sulfides, producing local ^{34}S-enrched signatures.

Key words: sulfides, magmatic-hydrothermal deposit, gold deposit, Darasun, sulfur isotopes, LA-ICP-MS

Introduction

The Darasun goldfield stands out regionally as a key representative of gold-quartz-tourmaline type of mineralization, connected with the granitoid magma, which is characteristic of the Transbaikalia region (within the Mongolo-Okhotsk orogenic belt) (Zorin et al. 2001). The Darasun goldfield comprises three deposits: Darasun (228 tons of Au), Talatui (27 tons of Au) and Teremkyn (10 tons of gold), which have been studied for over 100 years (Zenkov 1946; Sakharova and Nekrasov 1964; Timofeyevsky 1972). These deposits are identified as a high-sulfide intrusion-related Au-As-Pb-Zn-Cu-Bi-Ag ones with some signs of

porphyry systems (Zorin et al. 2001), spatially distributed related to the source of magmatic fluid. Stable oxygen and carbon isotope studies indicate magmatic origin of the ore-forming fluids at the Darasun deposit (Prokofiev et al. 2010a), consistent with the model of a unified hydrothermal-magmatic mineralization system linking these three deposits (Prokofiev et al. 2010b).

Previous fluid inclusion studies (Prokofiev et al. 2000, 2004, 2007, 2010b) showed that ore formation temperatures decrease and fluid composition evolves systematically from the close-to-source Talatui towards the most distal Darasun. The disseminated ores of the Talatui deposit were formed at the highest temperatures (610–133 °C), Teremkyn ores were precipitated at intermediate temperatures (466–188 °C), and Darasun veins at the lowest temperatures (430–120 °C). Along this transect, the fluids composition also changed, with Talatui being relatively enriched in less volatile components, such as Cl, SO_4, Ca, Br, and Sr, whereas Darasun is relatively enriched in more mobile and volatile species, such as CO_2, CH_4, HCO_3, As, Hg, Te, Se, and Li (Prokofiev and Selector 2014). Near the magmatic source, fluid boiling resulted in phase separation into brine and a lower-density volatile-rich phase (barbotage). This volatile phase migrated to greater distances from the fluid and metal source, enriching the peripheral parts of the ore-magmatic system in volatile components.

At the same time, the Darasun mineral district shows features that are not explained by regional cooling and phase separation alone. The Teremkyn deposit shows evidence for stronger interaction with meteoric waters (Prokofiev et al. 2012; Baksheev et al. 2015), while Darasun contains a sulfate-bearing assemblage with an anhydrite-rich core and gypsum cap (Slolyarov 1980; Grinenko et al. 2004), together with multiple generations of pyrite in its ore assemblages (Timofeyevsky 1972). These features provide an opportunity to examine how regional cooling and fluid evolution interacted with local changes in redox state, meteoric-water influx, sulfate precipitation and reduction, and late sulfide remobilization, and how these processes were recorded in the sulfide mineralogy, trace element compositions and sulfide isotope signatures.

In this study, we investigate trace element composition and sulfur isotopes in pyrite, chalcopyrite, arsenopyrite, galena, sphalerite and sulfosalts from Talatui, Teremkyn, and Darasun deposits. We evaluate the regional geochemical changing of the system using variations in Co, Ni, Cu, Zn, As, Ag, Sb, Sn, W, Au, Pb, Bi and other trace elements in sulfides along Talatui-Darasun transect. We then examine three pyrite generations at the Darasun deposit to distinguish the main stages of sulfide formation from later remobilization and recrystallization using laser ablation inductively coupled plasma mass spectrometry (LA-ICP-MS) technique. Finally, we compare sulfide and sulfate sulfur isotope compositions ($\delta^{34}S$) to constrain the sulfur source and the processes responsible for their spatial variation, including the origin of the bimodal $\delta^{34}S$ distribution at the Darasun deposit and its relationship to the anhydrite-bearing zone.

Geological Background

The Darasun goldfield deposits formed as a part of the large magmatic-hydrothermal system, engendered by granitoid magmatism of the Amudzhikan (Amudzhikan-Sretensk) complex (J_3-K_1)

(Timofeyevsky 1972; Prokofiev et al. 2000). The Darasun goldfield is confined to the main suture of the Mongol-Okhotsk belt, the tectonic structure that hosts numerous other gold deposits connected with granitoid magmatism of the Amudzhikan complex (Fig. 1a), underscoring the role of the deep-seated zones in controlling their origin (Zorin et al. 2001). These three deposits (Darasun, Talatui, and Teremkyn) are located at varying distance from the quartz syenite intrusion of the Amudzhikan complex (Fig. 1b). The Darasun goldfield mineralization is associated with polyphase subvolcanic granite porphyry and granodiorite porphyry stocks and dykes of the Amudzhikan complex. The constrained age for the most peripheral and latest stock of the Darasun deposit is 160.5 ± 0.4 Ma (Chernyshev et al. 2014).

The subvolcanic and intrusive bodies of the Amudzhikan complex are hosted by different Mesozoic and Paleozoic intrusive complexes (Fig. 1). The region's oldest metamorphosed gabbroids of the Kruchininsky complex (D_3) have been intruded by granitoids of the Krestovsky (D_3) and Olekminsky (C_1) complexes, which are common in the southwest of the region. The U-Pb zircon dating (Kovach et al. 2018; Larin et al. 2024) confirms their similar geochemistry (Kazimirovsky et al. 1993) and their age ranging from Late Devonian to Early Carboniferous age (Fig. 1b). Host rocks are altered: the mafic rocks around the ore zones are listvenitizised (Fe-Mg carbonates + quartz + fuchsite ± pyrite), and felsic rocks are beresitized (quartz + sericite + ankerite + pyrite) at all deposits.

The Talatui deposit locates closest to the quartz syenite Amudzhikan intrusion and is hosted by the metamorphosed gabbroids of the Kruchininsky complex (Fig. 1b), which were significantly altered during later Amudzhikan magmatism and accompanying ore-forming process (Prokofiev et al. 2007). The host sequence contacts with the Amanansky granitoids (T) to the northwest and the diorites of the Krestovsky complex to the south (Fig. 1b). The Talatui stockwork-disseminated mineralization (with <15 vol.% of sulfides) forms lenticular and vein-like zones of northwest strike, extending up to 2000 m along strike and 200-500 m downdip, with Au concentrated in ore shoots at structural intersections. There are two main ore areas – Zone 2 and Zone 3, which are outlined within the Talatui deposit as the most productive. Three stages of mineralization are recognized at the Talatui deposit (Prokofiev et al. 2007, 2010b). The earlier stage is characterized by quartz, epidote, orthoclase, phlogopite, magnetite, tourmaline and pyrite. The second stage is dominated by quartz-pyrite-chalcopyrite assemblages with anhydrite, barite, muscovite and sphalerite. The late stage consists primary of carbonates. The disseminated ores in the Zone 3 are hosted by orthoclase- and phlogopite-bearing metasomatic rocks, which corresponds to the first higher temperature stage of ore formation. Ore veins in the Zone 2 are richer in chalcopyrite (up to the occurrence of chalcopyrite massive veinlet orebody) and are more enriched in Au (Prokofiev et al., 2007). Generally, the Talatui ores are distinguished by their mineralogically simplest composition, relative to Teremkyn and Darasun ores. Fluid inclusion studies indicate that Talatui formed at the highest temperatures among the three deposits, ranging from 610 to 133 °C (Prokofiev et al. 2010b, 2023). Consistent with the high-temperature origin, native gold at Talatui exhibits the highest fineness, ranging from 997 to 777 ‰.

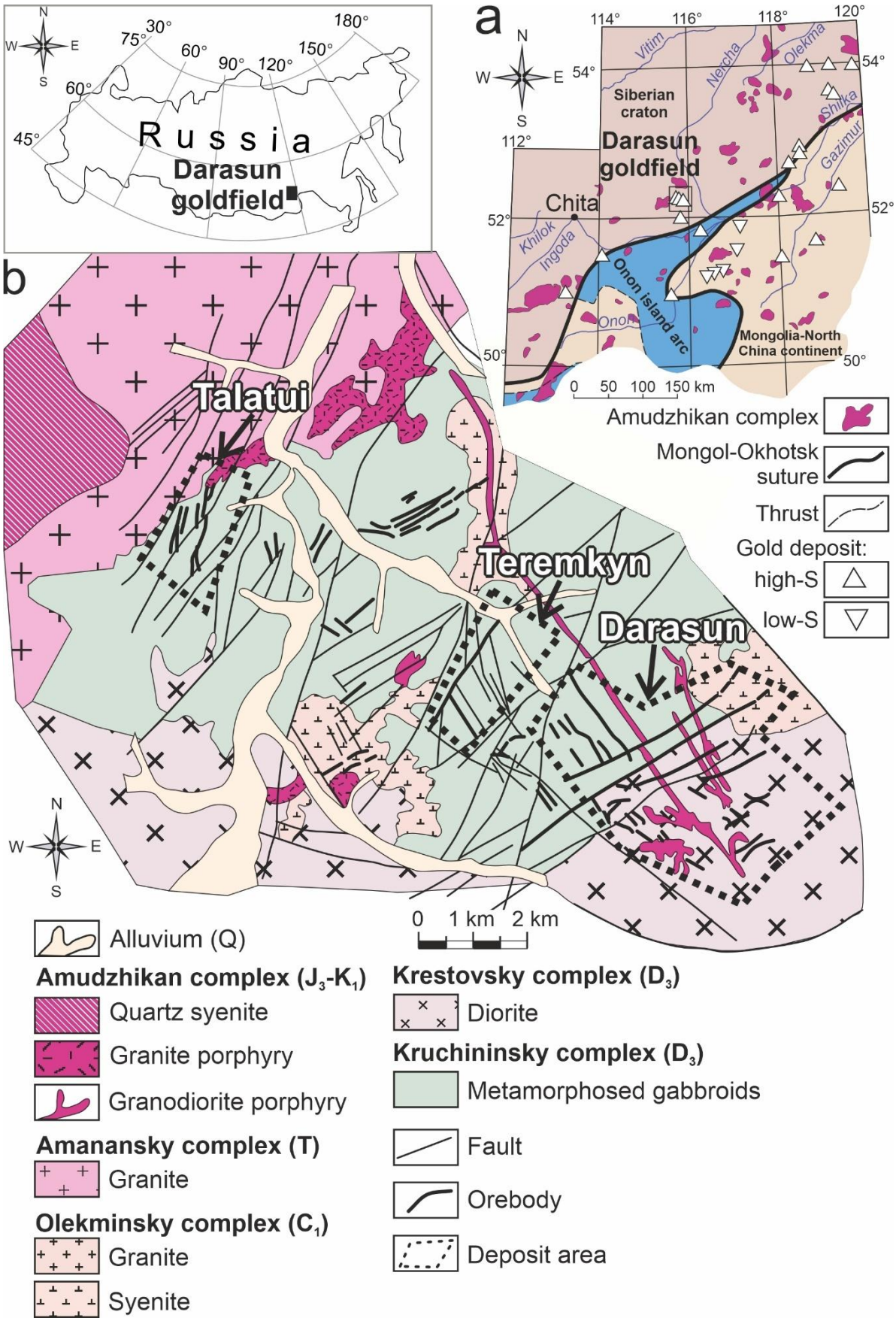


Fig. 1. Geological scheme and position of the Darasun goldfield. **a** Geological scheme of the Eastern and Central Transbaikalia (modified after Zorin et al. 2001). **b** Geological map of the Darasun goldfield (modified after Prokofiev et al. 2004).

The Teremkyn deposit is located 7 km from the Amudzhikan intrusion at intermediate position between Talatui and Darasun deposits (Fig. 1b). In contrast to mostly disseminated-style of mineralization in Talatui, Teremkyn is characterized by a series of stacked, shallow and steeply dipping tourmaline-quartz-sulfide veins (with 20 vol.% of sulfides), which are hosted by metamorphosed gabbroids of the Kruchininsky complex (Fig. 1b). There are veins named: Vein 2, Gornyatskaya, Skorostnaya, Komsomolsk, Vera, Dochernaya, Nadezhda, Zolushka, Postnaya, Pologaya, Zagadochnaya, Severnaya, Vesennyaya, and Okhristaya. These veins are localized beneath subhorizontal dykes of the Amudzhikan complex, which acted as structural screens and created a tiered architecture that controlled the vertical distribution of mineralization. Three stages of mineralization have been established at Teremkyn (Prokofiev et al. 2004). The early stage is represented by quartz-tourmaline-pyrite assemblages. The productive stage is quartz-pyrite-chalcopyrite, similar to that found at Talatui, but notably more diverse than at Talatui, featuring abundant Bi minerals (native Bi, bismuthinite, aikinite, tetradymite), sulfosalts of Ag, Bi and Pb, along with galena and more common sphalerite. The late stage consists mostly of carbonates. According to fluid inclusion data, the Teremkyn deposit formed at temperature ranging from 466 to 118 °C (Prokofiev et al. 2004). This is reflected in lower fineness of Au, which ranges from 928 to 655 ‰.

The Darasun deposit is the most distant from the center and the largest element of the Darasun goldfield magmatic-hygrothermal system, located 12 km from the quartz syenite intrusion of the Amudzhikan complex. The deposit is centered on a Amudzhikan subvolcanic granodiorite porphyry stock with the explosive breccia pipes (Figs. 1b, 2a). The explosive breccia pipes are composed of fragments of sericitized granodiorite porphyries cut by quartz veinlets with tourmaline, sericite, carbonates, pyrite and chalcopyrite. The leucocratic dykes of the Amudzhikan complex, which intersect the earlier mafic dykes, are common throughout the deposit area (Fig. 2a). These subvolcanic formations and sulfide veins are hosted by the contact metamorphosed intrusive rocks of Krestovsky, Olekminsky and Kruchininsky complexes. As a whole, structure of the Darasun deposit is confined to the contact between the gabbroids of Kruchininsky complex (NW part) and the granitoids of Krestovsky complex (SE part) (Figs. 1b, 2a). The Darasun deposit consists of approximately 200 steeply dipping veins, interconnected with the faults and/or granodiorite porphyry stock and/or each other (Fig. 2). These veins are characterized by small thickness (on average 10–20 cm) but considerable strike length (up to 2 km). The more extensive veins (Glavnaya, Novo-Kuznetsov, Svintsovaya, Electric-II, Novo-Electric, Futbolnaya, Lagunov, Iskra, Polymetall) often strike northeast, parallel to contact zone, while minor veins typically cut across them at a perpendicular orientation (5th Electric, Sblizhennaya, Morozov, Sentyabr, Pyrrhotite, etc.) and extend to the northwest, or located in the same position relative to the faults (Southwest veins, Sannikov, Ulybka, Nagornaya veins, Lebedev veins, Vein 156, Razvedochnaya) (Fig. 2a). The latter is more common in the eastern part of the Darasun deposit (Fig. 2a).

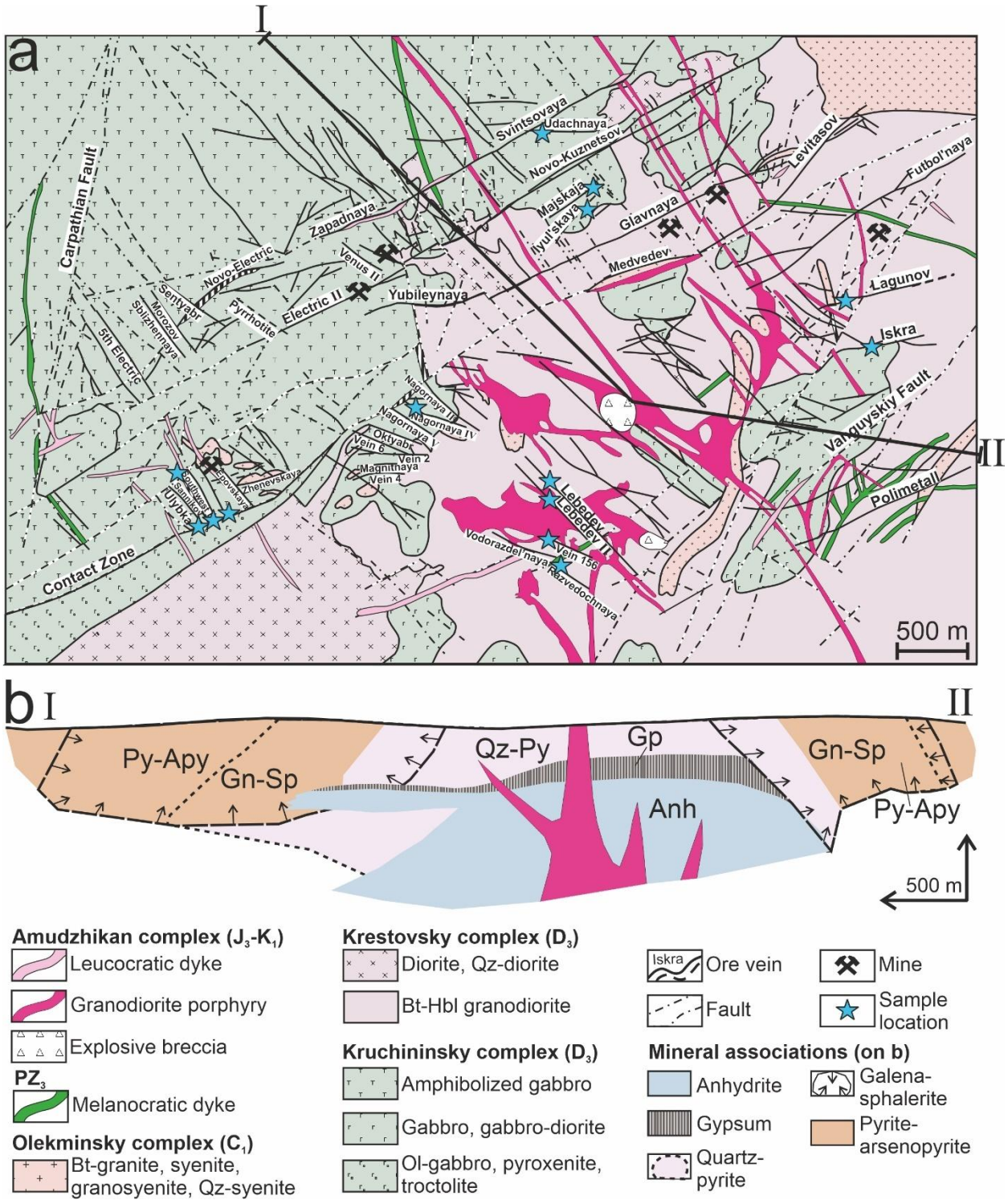


Fig. 2. Schematic geological map and cross-section of the Darasun deposit. **a** Schematic geological map with ore veins and locations of the studied samples (modified after Prokofiev et al. 2010a). **b** Schematic cross-section (the line I-II is shown on Fig. 2a) with mineralogical zoning (modified after Stolyarov 1980).

The mineralogy at the Darasun deposit ores is the most complex among three deposits. Different studies distinguished up to 7 main stages of formation of ores (Zenkov 1946; Timofeyevsky 1972). According to (Prokofiev et al. 2010b), only three main stages may be really recognized and each contain numerous sub-associations. The earlier stage includes quartz, tourmaline and pyrite. The productive stage

is characterized by abundant arsenopyrite, which is a key distinguished feature of the Darasun deposit, along with chalcopyrite, sphalerite, galena, pyrrhotite, and a wide array of sulfosalts and Bi-tellurides. The late stage consists of quartz, carbonates, zeolites and fluorite. A concentric mineralogical zoning is evident around the stock, with quartz-tourmaline assemblages dominant in the center, pyrite-arsenopyrite assemblages on the periphery and galena-sphalerite ores predominant between them (Fig. 2b; Timofeyevsky (1972)). Pyrrhotite-chalcopyrite ores are more common in the Western Zone of the deposit (area around vein Pyrrhotite) (Sakharova and Nekrasov 1964).

Anhydrite and gypsum-bearing associations with pyrite, chalcopyrite, and molybdenite are common in the central part and were intersected by five boreholes at depths 300–400 m (Slolyarov 1980). Gypsum-rich mineralization forms a "cap-like" structure above the anhydrite-rich dome (Fig. 2b). In this dome, sulfates, along with quartz, become the principal vein minerals and also occur in proportion up to 10% in the inter-vein space of the altered host rocks (Slolyarov 1980). This anhydrite-gypsum zone is spatially related to the development of argillitic and quartz-sericite alteration in the overlaying host rocks. These associations are believed to be formed at the earlier stage at high fO_2 (as also indicated by the abundance of hematite and magnetite veins) and closely interconnected with the granodiorite porphyry dykes, as the sulfate dome copies the elongation of the dykes and also expanses downwards (Slolyarov 1980). Fluid inclusion studies demonstrate the lowest formation temperatures of Darasun ores among three deposits, ranging from 430 to 120 °C (Prokofiev et al. 2023). Gold fineness (ranging from 896 to 590 ‰) is lowest at Darasun, while the reserves are the highest.

Samples and analytical methods

Samples description

The studied samples (n=92) were collected during multiannual expeditions of the Institute of the Geology of Ore Deposits, Petrography, Mineralogy, and Geochemistry, Russian Academy of Sciences (IGEM RAS) (1974–2015 years) and Vinogradov Institute of Geochemistry, Siberian Branch, Russian Academy of Sciences (1981–1999 years). Brief descriptions and locations of the studied samples are provided in Supplementary table S1. All studied samples from the Talatui deposit consist of disseminated ores collected mostly from the outcrops and loose fragments at the Zone 2 and Zone 3 in open pits and the underground mine. The studied collection from Teremkyn and Darasun contain samples from open pits and outcrops in the underground mines. The sampled fragments at the Teremkyn deposits were collected from veins: Vein 2, Gornyatskaya, Komsomolsk, Skorostnaya, Vera, Dochernaya and Nadezhda – all from the Central Zone of the Teremkyn deposit (see map in Prokofiev et al. (2004)). The sampling locations in the Darasun deposit are shown in Fig. 2a. In this work, only two samples with anhydrite and gypsum were examined, as they were the only samples with sulfates in the available collection. The boreholes material from the central part of the Darasun deposit with abundant anhydrite (see Geological background), which is currently lost, was investigated by (Slolyarov 1980; Grinenko et al. 2004). This information and analyses were employed to conduct a more comprehensive examination of the matter, which is present in Discussion.

The polished sections of the samples from the three deposits were examined in details under a petrographic microscope. The most interesting fragments were cut out and embedded into the six polished epoxy blocks of one inch (25 mm) in diameter for efficient analysis.

EPMA

Concentrations of the major and trace elements in arsenopyrite, pyrite, fahlore and other sulfosalts were determined by an JEOL JXA 8200 electron probe microanalyser (EPMA) at the IGEM-Analitika analytical center. The EPMA is equipped with five wavelength spectrometers. Measurements were operated at 20 kV accelerating voltage, 20 nA beam current per Faraday cylinder, and 1 μm beam diameter. The results of analyses are provided in Supplementary table S2. A detailed description of the parameters and standards for measuring various elements in minerals is given in the Supplementary table S3.

LA-ICP-MS

Concentrations of trace elements: ^{57}Fe, ^{59}Co, ^{60}Ni, ^{63}Cu, ^{66}Zn, ^{69}Ga, ^{72}Ge, ^{75}As, ^{77}Se, ^{95}Mo, ^{107}Ag, ^{111}Cd, ^{115}In, ^{118}Sn, ^{121}Sb, ^{125}Te, ^{182}W, ^{197}Au, ^{202}Hg, ^{205}Tl, ^{208}Pb and ^{209}Bi in pyrite, chalcopyrite, arsenopyrite, galena, sphalerite, fahlore and other sulfosalts were determined by LA-ICP-MS at the IGEM-Analytica analytical center. The part of pyrite LA-ICP-MS data has been published and discussed in details in (Prokofiev et al. 2022, 2023). This study provides the further research of pyrite and other minerals and reconcile the previously published data, based on, in total, 736 analyses of individual sulfides. The LA-ICP-MS system is consisted of a New Wave UP-213 (Nd:YAG) laser with an Thermo XSeries2 quadrupole ICP-MS. The LA-ICP-MS analysis of sulfides was performed in spots and profiles using a laser beam of different diameters (depending on the targets and the phase size from 50 to 80 μm), at a pulse frequency of 10 Hz, a beam density of 2.5 J/cm^2, and a burn rate of 10 μm/s for profiles. The acquisition time in the spot mode was 30 s for the background, 60 s for the mineral analysis, and 30 s of washout. Each line profile preceded 30 s of background. The carrier gas was a mixture of helium with the addition of 6% hydrogen (0.6 l/min) and argon (0.75 l/min) at a flow rate of 0.65 l/min. The mass spectrometer was calibrated using multielement calibration solutions. International reference standards were used for calibration and calculations: UQAC-FeS_1 pressed sulfide with added trace elements (Savard et al. 2018), manufactured at Chicoutimi University (Canada), and MASS-1 polymetallic sulfide (U.S. Geological Survey). The calculations were performed in the Iolite program, using the ^{57}Fe (for pyrite, chalcopyrite and arsenopyrite) and ^{33}S (for galena, sphalerite, fahlore and other sulfosalts) contents as an internal standard. Micro-impurities in pyrite were calculated based on Fe content, measured in (Prokofiev et al. 2023) and in this work using EPMA. Chalcopyrite, galena and sphalerite were calculated on the internal standards concentrations according to their stoichiometric formulas (30 wt. % of Fe, 13.4 wt.% of S, 32.9 wt.% of S, respectively). Trace elements in sulfosalts – mostly cosalite, galenobismitite and minor fahlore (tetrahedrite), which were previously identified by EPMA, were calculated using 16 wt.%, 16 wt.% and 25.5 wt.% of S respectively. The LA-ICP-MS data on arsenopyrite were quantified using Fe content as an internal standard, pre-obtained by EPMA. Detection limits for LA-ICP-MS analyses were calculated as three sigma multiplied by the blank background values. The LA-ICP-MS results for sulfide analysis are

presented in Supplementary table S4, and the standard measurement results are presented in Supplementary table S5.

The LA-ICP-MS mapping was performed by burning (ablating) a series of parallel lines on the sample surface to form a rectangular grid. Background was measured for 30 seconds before each new line. The following mapping parameters were used: beam diameter of 15 μm, pulse frequency of 10 Hz, beam density of 2.5 J/cm^2, scan speed of 10 μm/s, and interline spacing of 7.5 μm. Each analysis included all the isotopes listed above, with a dwell time of 10 ms. UQAC-FeS1 and MASS-1 standard samples were analysed at the beginning and end of the map. Data processing was performed using Iolite software.

Sulfur isotope analysis

Sulfur isotope data were obtained from the same grains and spots analysed by LA-ICP-MS after polishing (n=31 analyses) by isotope ratio mass spectrometry (IRMS) with laser ablation sampling and fluorination in the Laboratory of Stable Isotopes of the Far East Geological Institute, Russian Academy of Sciences (Velivetskaya et al. 2019). The $^{34}S/^{32}S$ isotope ratio was measured using a Thermo Fisher MAT-253 multicollector mass spectrometer using the Isodat Acquisition program. When exposed to femtosecond ultraviolet laser radiation (NWR Femtosecond UC with laser Pharos 2mJ-200-PP and harmonics module HE-4Hi-A), an aerosol sulfide particle formed, which reacted with BrF_5 and were converted into SF_6 gas when passing through a heated reactor in a helium flow. Faraday cups of the multicollector allow synchronous measurement of the masses of 127 ($^{32}SF^{5+}$), 128 ($^{33}SF^{5+}$) and 129 ($^{34}SF^{5+}$). During the measurements (700 sec), the sample signal was compared with the standard SF_6 gas signal, which was supplied in the automatic mode as 4 pulses before and 3 pulses after the sample analysis. A laser frequency was 100 Hz, a beam diameter was 100 μm, a crater depth was ~ 40 μm on average. The results are presented as $\delta^{34}S$ values relative to the VCDT standard: $\delta^{34}S = (^{34}S/^{32}S)$ sample / $(^{34}S/^{32}S)$ std – 1. For an in-house standard, a $\delta^{34}S$ value of +17.45‰ was verified against the International Atomic Energy Agency (IAEA) standards (IAEA-S-1, IAEA-S-2, IAEA-S-3 and NBS-123). Uncertainty of $\delta^{34}S$ analyses was found as ± 0.15 ‰ (1σ) from the long-term (>3 yr) reproducibility of the in-house standard. Additional sulfur isotope analyses of $\delta^{34}S$ values relative to the VCDT standard (n=40) were obtained from monomineralic fractions using MI-1311 mass spectrometer at IGEM RAS (analyst L.P. Nosik) and at the Central Research Institute of Geological Prospecting for Base and Precious Metals (FSBI TsNIGRI) using an MI-1201 mass spectrometer (analyst S.G. Kryazhev). The literature data (Prokofiev et al. 2000, 2007; Grinenko et al. 2004) were also taken into account in this paper and the whole compilation is presented in Supplementary table S6.

Results

Petrographic observations

In the Talatui deposit, the textural features of disseminated sulfides vary significantly depending on the nature of the host matrix. Sulfides hosted by altered (epidotized, chloritized) gabbroids occur as thin

278 veinlets that surround and cut through blocks of the altered mafic rock (Fig. 3a). The sulfides assemblage
279 is dominated by pyrite-chalcopyrite intergrowths, in which pyrite commonly forms distinct cubic grains
280 (0.5–1 mm in size) cemented by chalcopyrite. By contrast, sulfides associated with quartz-tourmaline veins
281 exhibit more euhedral grain shapes, scattered within the vein matrix (Fig. 3b). In the Zone 2, the proportion
282 of chalcopyrite exceeds that of pyrite, whereas pyrite prevails in the Zone 3 (Fig. 3a, b; Supplementary
283 table S1). Veinlet pyrite occurs in magnetite ores (sample № 50/01), forming elongated ribbons up to 0.5
284 mm in thickness. Sample 55/07, which hosts a texturally distinct pyrite-chalcopyrite assemblage, also
285 contains Bi-Pb sulfosalt mineralization (~1.5 mm in size), intergrown with quartz, carbonates and other
286 sulfides. Furthermore, native gold and pyrite are closely spatially associated.
287 The samples from the Teremkyn deposit consists of quartz, tourmaline, carbonate, epidote, pyrite,
288 chalcopyrite, galena, sphalerite, cosalite, fahlore, marcasite, and magnetite, occurring in variable
289 associations and proportions (Fig. 3c-e). The primary quartz-tourmaline-pyrite assemblage is largely
290 overprinted by later polysulfide mineralization. The superimposition of multiple sulfide formation stages
291 complicates the identification of pyrite, which may form during any of these stages. Pyrite occurs as distinct
292 cubic grains up to 5 mm in size, frequently forming chain-like aggregates within veins or intergrown patches
293 3–5 mm across (Fig. 3c, d). This pyrite is rimmed by quartz and tourmaline and defines discrete pyrite-rich
294 zones in samples that also contain later sulfides in the discrete zones (Fig. 3c, d). Only three studied samples
295 host a singular pyrite-chalcopyrite assemblage – a texture feature characteristic of Talatui ores. Overall, the
296 studied Teremkyn samples are characterized by the widespread occurrence of galena, sphalerite, and
297 fahlore, which form intergrowths with chalcopyrite and with each other. Secondary fine-grained pyrite-
298 marcasite intergrowths, which likely replace pyrrhotite, occur in sample № 249T82, associated with
299 magnetite and galena (Fig. 3e). Native gold is commonly associated with pyrite and fahlore.
300 The Darasun ores exhibit the greatest diversity in sulfide mineral assemblages, encompassing all
301 previously listed minerals and distinguished by the abundance of arsenopyrite (Fig. 3). Most of the Darasun
302 ore samples, like those from Teremkyn, do not exhibit a single stage of ore formation but instead contain
303 superimposed zones of contrasting mineral associations. Massive pyrite 1 (Py1), which is restricted to
304 tourmaline-quartz assemblages, represents the least common association in the studied samples and occurs
305 in coarse commonly cubic grains up to 6 mm in size. Such primary associations are typically crosscut by
306 later pyrite-arsenopyrite veins with chalcopyrite (Fig. 3f), galena, sphalerite, fahlore and other sulfosalts –
307 minerals that also occur independently in variable proportions (Fig. 3f, g). Pyrite 2 (Py2) demonstrates
308 considerable variations in both grain size (typically up to 1.5 mm) and morphology, ranging from anhedral,
309 near-seamless intergrowths with arsenopyrite to discrete cubic crystals embedded in chalcopyrite or galena.
310 It also can rim earlier Py1. Pyrite 3 (Py3) is distinguished by its finer grain size (up to 0.05 mm, but
311 frequently 50 μm) and less euhedral form of grains, occurring as angular fragments disseminated within
312 chalcopyrite and often associated with tiny grains of fahlore. In the Teremkyn samples, pyrite 4 (Py4) and
313 marcasite likely replaced primary pyrrhotite. Such pyrite-marcasite assemblages are absent in the samples
314 from the Darasun deposit, although their presence in Darasun was previously reported by (Timofeyevsky

1972). Arsenopyrite occurs in intergrowths with pyrite grains and forms the cleaved acicular crystals, that are commonly elongated in one or several directions. Galena is predominantly found in intergrowths with arsenopyrite, fahlore, magnetite, sphalerite, and only rarely with pyrite. Native gold is typically associated with pyrite, Bi-tellurides, fahlore and other sulfosalts.

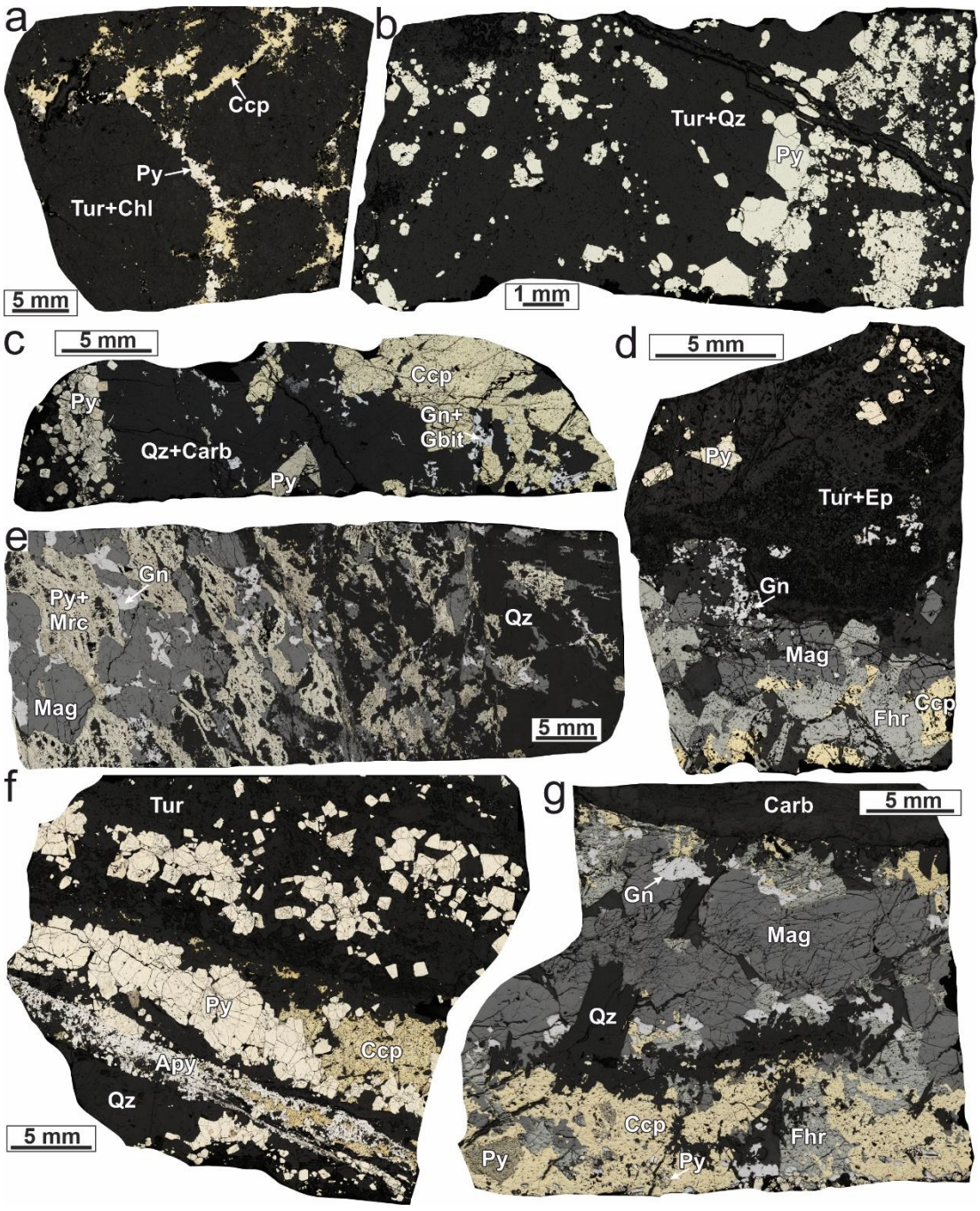


Fig. 3. Representative microphotographs of sulfide ore samples from the Talatui (a-b), Teremkyn (c-e), and Darasun (f-g) deposits. **a** Pyrite-chalcopyrite ore veinlets in tourmaline-chlorite matrix (sample № 147-05). **b** Chains of subhedral cubic pyrite grains dispersed within a quartz-tourmaline vein (sample № 4211Tl). **c** Quartz-carbonate vein fragments cemented by crushed, altered gabbro, hosting zones of cubic pyrite and chalcopyrite with galena-galenobismutite intergrowths and carbonate (sample № 2425Sht82). **d** Altered

gabbro containing magnetite and carbonates, with patches of cubic pyrite grains, galena and chalcopyrite-fahlore intergrowths (sample № 3339Sht). **e** Quartz vein containing later carbonate, magnetite, pyrite-marcasite and galena (sample № 249T82). **f** Zoned sulfide-quartz-tourmaline vein exhibiting patches of cubic pyrite grains, succeeded by massive pyrite with chalcopyrite, followed by an arsenopyrite-chalcopyrite zone (sample № shv80). **g** Quartz-carbonate vein hosting magnetite, chalcopyrite, fahlore, galena, and later pyrite (sample № 775Dr86).

Major and trace elements in sulfides

Pyrite

Pyrite from three deposits differs in trace element concentrations. Our data corroborate the earlier inference of Prokofiev et al. (2023) that pyrite from high-temperature ores at Talatui is relatively enriched in Co, Se, and W. Moreover, our data revealed a consistent enrichment of Talatui pyrite in Ga, Ag, Cd, Te, coupled with depletion in As, Sn, Au, Pb, and Bi, relative to pyrite from the Teremkyn and Darasun ores (Table 1). Gold is positively correlated with As in Teremkyn, but no correlation is observed for As and Au in Talatui pyrite (Fig. 5a). The median Co/Ni ratio in pyrite descends sharply in Teremkyn (Co/Ni=0.3) and Darasun (Co/Ni=0.5) in contrast with Talatui (Co/Ni=10). Cobalt content does not show any consistent correlations with Ni (Fig. 5b). Whereas, the median As/Co ratio in pyrite gradually increases from Talatui (As/Co=0.54), to Teremkyn (As/Co=16.9) and further to Darasun (As/Co=81.4).

Different morphological types of pyrite from Talatui do not demonstrate any discrepancy in trace elements concentrations, despite the representative sampling (n=198; Supplementary table S4). Time-resolved LA-ICP-MS depth profiles reveal that Co and Ni are heterogeneously distributed within pyrite grains from the Talatui deposit, where they tend to correlate with each other, although not invariably. Pyrite from the Zone 3 is characterized by higher concentrations of Co, Cu, Ga, As, Se, In, Au, Bi, and pyrite from the Zone 2 is enriched in Ni, Zn, Ag, and Cd.

The Teremkyn samples largely contain distinct cubic pyrite grains, similar to those observed in Talatui. In general, Teremkyn pyrite exhibits the highest median Ni, As, and Bi concentrations and the lowest Cu, Zn, Ga, Se, Ag, Cd, In, and Te comparing to pyrite from the Darasun and Talatui deposits (Table 1). The LA-ICP-MS time-resolved spectra demonstrate sporadic, non-correlative Zn-In and Bi peaks across the Teremkyn pyrite grains, as well as a lack of correlation between Co and Ni. The pyrite-marcasite aggregate from one sample № 249T82 (Fig. 3e) is distinguished by the lower Ni, Te and higher Ag, Sb, Tl, and Pb average concentrations, than pyrite from other samples (Supplementary table S4). Data on this later pyrite are excluded from the statistical data presented in Table 1. Trace elements are distributed relatively homogeneous within these pyrite-marcasite aggregates. The highest contents of Au were found in pyrite from sample 227Sht81 (up to 12.3 ppm) and sample 130-05 (up to 10.8; Supplementary table S4). Gold concentration in the Teremkyn pyrite correlates positively with As (R^2=0.49; Fig. 5a).

In general, the Darasun deposit pyrite is characterized by the lowest concentrations of Co, Ni, Ge, W and Tl, and the highest concentrations of Cu, Zn, In, Sn, Sb, and Au among pyrite from all three deposits (Table 1). According to the petrographic observations, pyrite in the Darasun deposit samples is pervasively

represented by three generations (Py1, Py2, and Py3). The LA-ICP-MS data show that three principal pyrite types exhibit distinct features in trace element concentrations (Figs. 4, 5, 6, 7). Pyrite 1 is characterized by higher concentrations of Co and Ni (Fig. 5b) and lower contents of Cu, Zn, Ga, Ag, In, Sn, Sb, Te, Au, Tl, Pb, and Bi compared to the other types of pyrite (Fig. 4). The median contents of Cu, Zn, Ga, Ag, In, Sn, Sb, Te, Tl, and Pb gradually increase from Py1 to Py2 and further to Py3 (Fig. 4). Pyrite 2 has the highest median concentrations of Au, As, Se, and Bi (Fig. 4), highest maximum Au and As (Fig. 5a) and highest As/Co ratio with median 911 and maximum 20000 (against median 1.67 in Py1). Gold concentrations in Py2 and Py3 correlates positively with As, however these elements do not correlate in Py1 (Fig. 5a). Median Co content in Py1 is comparable with the Talatui pyrite, whereas Ni is much lower (median Co/Ni=4.5). Median Co and Ni in the other pyrite types in the Darasun deposit are an order of magnitude lower than those in Py1 and in pyrite from Teremkyn and Talatui. Median Au contents in all types of the Darasun deposit pyrite exceed those in pyrite from Teremkyn and Talatui. The elevated concentrations of As and Se in Py2 do not surpass those in pyrite from other deposits. Median Bi content in Py2 is higher than median Bi in pyrite from Teremkyn and Talatui.

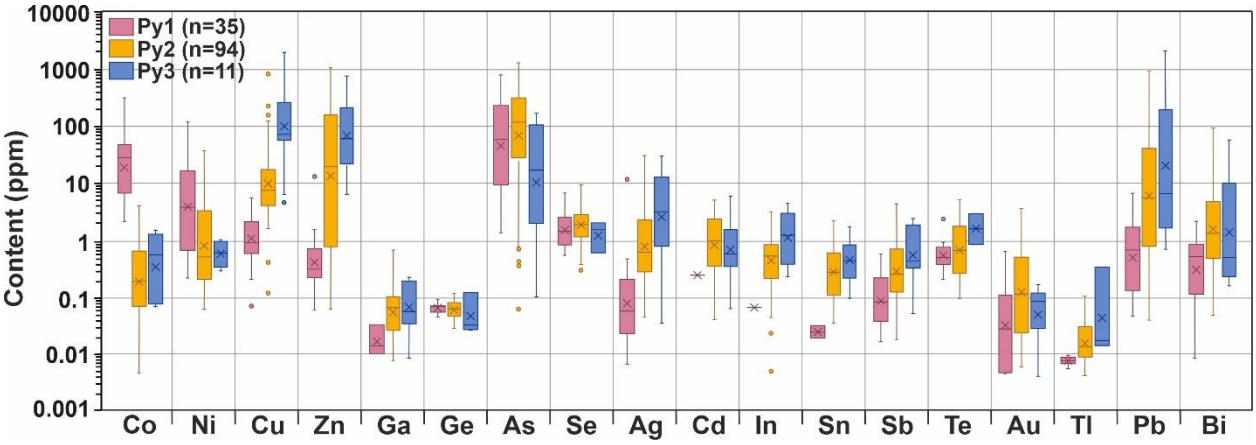


Fig. 4. Boxplots of trace element contents in three distinguished types of pyrite from the Darasun deposit.

Only two of the analysed samples contain all three types of pyrite grains simultaneously (samples 20Vd89 and 20Dr85 from the Lagunov vein). These samples represent a very common pyrite-arsenopyrite type of ore in the tourmaline-quartz-carbonate veins and contain Bi-Te sulfosalts. Although there are some differences in the distribution of specific elements in pyrite from these two samples, each type of pyrite shows almost the same characteristics (Figs. 6, 7). Py1 differs in higher Co content, but generally lower contents of other elements compared to the other types of pyrite (Figs. 6, 7). Trace elements in Py1 are heterogeneously distributed within the grains, likely enriching different zones. In Py1 from sample 20Dr85, the Au signal correlates positively with As and Bi, exhibiting a smooth intensity variation (Fig. 6); conversely, in Py1 from sample 20Vd89, the Bi signal proves uneven, and Au is below the limit of detection (not shown in the spectra in Fig. 7). Sporadically distributed low peaks of In-Zn-Ga are observed in Py1 from both samples, although these peaks are not as prominent as those observed in Py2 (Fig. 6). It is

especially clearly observed in Py1 – Py2 intergrowth in sample 20Vd89, where Py2 rims are distinguished by a greater number of the Zn-In-Ga inclusions and the higher intensity of their spiky signals (Fig. 7). The multiple and recurring peaks of Zn-In-Ga composition in Py2 are likely attributable to mineral micro-inclusions (probably sphalerite), given that the concentrations of In and Zn in this pyrite significantly surpass those in the associated chalcopyrite. In contrast, Py3 is characterized by the highest concentrations of Zn and In, even higher than those in the associated chalcopyrite, as well as elevated Cu compared to other types of pyrite (Figs. 6g, 7f).

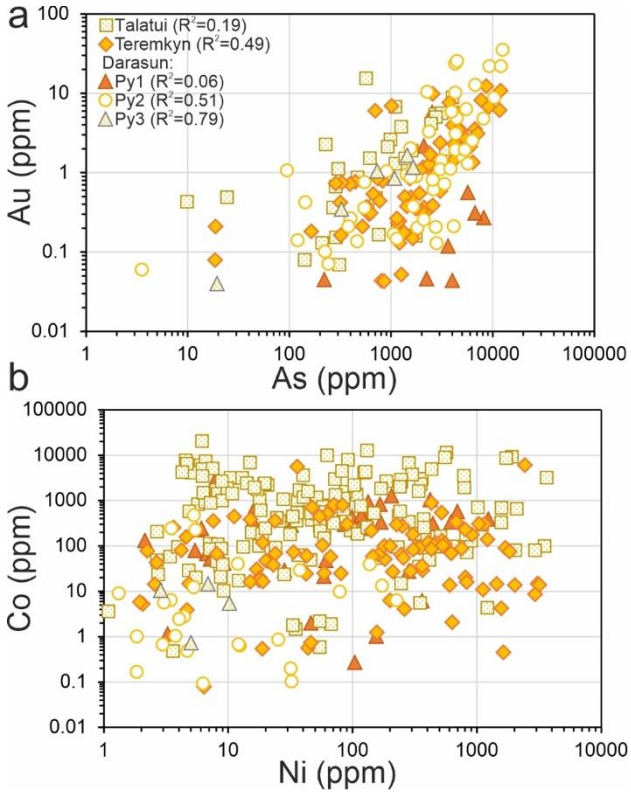


Fig. 5. Binary diagrams of As-Au (a) and Ni-Co (b) variations in pyrite from three deposits, the Darasun pyrite is subdivided into three types.

LA-ICP-MS mapping reveals a complex zonation of trace elements within the Py2 grains intergrown with arsenopyrite (Fig. 8). The central parts are relatively depleted in As, which is concentrated in distinct zones close to the grain boundaries. The widest zone of As enrichment in pyrite is confined to the contact with adjacent quartz. In this zone Co enriches the part with the lower As. Gold correlates positively with As contents in Py2 grain and occurs in pyrite both as solid solution and as micro inclusions of native Au (Fig. 8). The middle part of the Py2 grain contains the ring-like inner zone enriched in As, Pb, Bi, and Ag, which correlates with each other (Fig. 8). Copper shows the ambivalent distribution: enriching the outer zones, like Co, and also inner parts, where it correlates with the Zn-In-Sn inclusions (Fig. 8). The inclusions of Zn-In-Sn compounds are concentrated mainly in the central parts of pyrite grains.

414 **Table 1.** Summary of the LA-ICP-MS trace element data for pyrite, arsenopyrite, chalcopyrite and galena from the Darasun deposits.

Site	Mineral		Co	Ni	Cu	Zn	Ga	Ge	As	Se	Mo	Ag	Cd	In	Sn	Sb	Te	W	Au	Tl	Pb	Bi
												(ppm)										
Darasun	***n=145***	***n****	*87*	*82*	*134*	*93*	*38*	*66*	*143*	*76*	*0*	*109*	*44*	*58*	*53*	*98*	*51*	*4*	*69*	*36*	*103*	*101*
	Py	**AVR**	172	84.8	487	1068	0.86	0.64	1917	20.7		26.1	12.8	9.14	4.41	5.09	9.66	0.61	3.49	0.28	679	60.8
		MED	9.02	8.68	54.2	96.7	0.56	0.66	812	16.3		4.28	6.41	5.84	2.69	2.32	5.87	0.58	0.87	0.12	21.4	8.76
		GM	12.9	15.2	63.1	81.6	0.52	0.61	555	16.4		4.85	7.18	4.79	2.51	2.36	6.30	0.34	0.81	0.15	32.8	10.6
		MIN	0.05	0.60	0.68	0.59	0.08	0.27	0.61	2.98		0.07	0.40	0.05	0.19	0.16	0.93	0.05	0.04	0.04	0.39	0.08
		MAX	3231	1232	19491	10466	6.70	1.18	12509	89.7		304	58.2	44.6	22.0	42.8	50.2	1.22	35.3	3.30	21111	949
	n=84	***n****	*48*	*36*	*58*	*28*	*3*	*14*		*61*	*25*	*71*	*5*	*16*	*3*	*84*	*78*	*3*	*84*	*13*	*73*	*77*
	Apy	**AVR**	48.6	13.6	201	138	0.57	0.46	n.a.	16.5	4.25	84.3	3.45	0.40	0.68	147	124	0.20	58.0	2.62	875	75.5
		MED	3.23	6.16	19.0	6.52	0.46	0.44	n.a.	13.0	3.91	8.57	4.05	0.07	0.60	130	48.7	0.21	32.4	0.91	57.6	43.2
		GM	5.27	7.67	17.8	9.94	0.50	0.45	n.a.	11.7	3.37	7.07	2.72	0.14	0.67	124	56.1	0.19	27.3	0.84	87.2	33.5
		MIN	0.04	0.83	1.04	0.87	0.27	0.34	n.a.	2.36	0.72	0.12	1.00	0.03	0.58	30.9	1.68	0.12	0.54	0.03	2.54	1.14
		MAX	436	107	5351	1269	0.99	0.63	n.a.	59.3	8.51	4082	6.79	3.12	0.87	377	758	0.27	259	15.8	10839	552
	n=44	**n***	0	2		41	25	8	27	20	0	43	16	44	44	42	7	2	14	5	35	33
	Ccp	**AVR**		5.31	n.a.	999	1.79	5.41	1459	22.2		83.0	12.9	34.3	27.2	9.32	4.24	3.60	0.72	5.47	164	17.2
		MED		5.31	n.a.	360	0.93	2.73	240	19.2		33.9	5.49	29.6	23.7	3.78	3.04	3.60	0.55	3.87	18.3	3.48
		GM		4.96	n.a.	495	1.15	3.73	261	18.7		31.9	7.84	27.2	18.4	4.69	3.62	2.47	0.55	2.47	22.0	4.00
		MIN		3.42	n.a.	91.8	0.42	1.41	19.4	6.33		0.60	1.98	1.80	1.16	0.70	1.65	0.98	0.22	0.08	0.37	0.16
		MAX		7.19	n.a.	8460	8.04	19.4	29700	55.8		930	49.2	69.0	90.9	68.7	10.1	6.21	2.36	13.8	3750	345
	n=53	***n****	*0*	*0*	*51*	*32*	*0*	*0*	*53*	*44*	*0*	*53*	*53*	*0*	*39*	*53*	*49*	*0*	*16*	*53*		*53*
	Gn	**AVR**			183	9.81			255	106		5418	39.0		0.86	931	167		0.42	11.4	n.a.	8988
		MED			44.0	1.19			68.1	69.0		4210	40.2		0.77	551	99.3		0.35	2.31	n.a.	7620
		GM			73.4	1.48			124	80.5		4308	36.0		0.64	627	69.3		0.25	3.36	n.a.	3750
		MIN			6.17	0.50			5.19	8.80		1764	7.24		0.12	31.0	1.79		0.03	0.31	n.a.	11.2
		MAX			694	251			1420	262		19912	66.6		1.88	2770	427		1.77	79.1	n.a.	34023
Talatui	***n=198***	***n****	*193*	*184*	*109*	*84*	*5*	*90*	*196*	*108*	*7*	*85*	*8*	*10*	*9*	*46*	*39*	*24*	*63*	*12*	*170*	*135*
	Py	**AVR**	1518	277	184	97.2	1.41	0.89	512	40.9	10.1	38.0	9.52	5.16	7.20	117	13.0	9.56	1.27	41.6	161	13.2
		MED	358	54.5	17.1	4.19	0.84	0.89	169	26.3	9.81	4.33	7.75	2.60	0.41	0.85	10.1	2.24	0.18	0.20	1.63	1.82
		GM	310	62.9	18.0	7.44	0.85	0.85	178	27.2	10.0	4.27	6.19	1.72	1.13	1.09	8.66	2.50	0.29	0.71	2.04	1.78
		MIN	0.48	0.99	0.59	0.35	0.25	0.27	2.74	4.56	8.23	0.06	0.72	0.14	0.14	0.08	0.66	0.05	0.02	0.07	0.07	0.03
		MAX	20559	3647	7529	2195	4.22	1.87	7636	135	13.0	1056	23.3	13.9	34.6	5233	80.9	89.2	15.5	362	24030	390
	n=44	***n****	*12*	*6*		*42*	*5*	*0*	*41*	*28*	*0*	*43*	*37*	*39*	*42*	*26*	*7*	*0*	*7*	*7*	*36*	*42*
	Ccp	**AVR**	29.6	51.7	n.a.	2915	0.42		308	21.3		94.1	25.3	29.6	17.6	4.51	4.14		0.39	3.11	12.6	7.84
		MED	22.7	56.3	n.a.	1635	0.36		274	14.5		27.9	15.0	24.0	18.7	2.63	3.60		0.27	3.81	8.82	4.98
		GM	15.0	35.9	n.a.	1079	0.38		247	16.3		32.8	13.4	23.0	10.3	2.54	3.93		0.34	1.33	9.94	5.67
		MIN	1.08	9.63	n.a.	116	0.23		26.4	4.65		3.66	2.07	8.16	0.64	0.25	2.85		0.19	0.13	2.70	1.53
		MAX	83.1	92.1	n.a.	28500	0.65		1227	83.1		558	246.0	99.0	57.8	17.7	6.90		0.65	6.99	51.0	51.3
Teremkyn	***n=101***	***n****	*91*	*91*	*88*	*58*	*13*	*18*	*98*	*28*	*12*	*67*	*12*	*20*	*6*	*63*	*38*	*30*	*87*	*46*	*95*	*90*
	Py	**AVR**	252	429	57.7	117	0.24	0.96	2123	8.89	1.94	17.2	6.75	4.84	0.99	4.66	7.18	0.78	1.63	2.02	474	46.4
		MED	62.9	91.3	13.6	3.72	0.18	0.97	1279	6.81	1.51	3.49	4.60	1.09	0.62	1.16	4.79	0.49	0.44	0.40	29.3	11.5
		GM	43.6	96.0	18.2	7.46	0.19	0.88	910	6.67	1.66	3.98	4.24	1.57	0.57	1.55	4.98	0.54	0.57	0.54	38.4	7.29
		MIN	0.08	0.77	1.30	0.15	0.05	0.23	6.32	0.48	0.46	0.07	0.57	0.15	0.12	0.03	0.92	0.20	0.03	0.04	0.55	0.06
		MAX	6045	3171	749	1200	0.68	1.66	11951	32.1	3.63	141	18.3	38.6	3.35	89.7	24.4	5.39	12.3	18.8	9672	939

	n=31	***n****	*8*	*4*		*28*	*4*	*0*	*20*	*8*	*1*	*31*	*17*	*31*	*23*	*26*	*6*	*2*	*8*	*7*	*22*	*25*
	Ccp	**AVR**	7.88	68.6	n.a.	546	0.45		215	14.1	10.5	44.2	11.4	43.9	1.72	3.74	2.59	1.89	1.30	10.4	425	34.7
		MED	1.32	20.6	n.a.	284	0.30		203	14.4	10.5	17.2	7.11	32.7	1.11	2.93	2.21	1.89	0.58	0.75	21.4	6.66
		GM	3.13	21.6	n.a.	246	0.38		154	13.3	10.5	19.6	8.02	38.5	1.26	2.84	2.43	1.04	0.79	1.55	38.0	8.09
		MIN	1.04	2.34	n.a.	12.3	0.23		19.8	6.75	10.5	2.07	1.53	22.6	0.38	0.44	1.47	0.31	0.18	0.24	1.68	1.16
		MAX	36.3	231	n.a.	6600	0.96		776	21.3	10.5	225	46.2	106	10.2	9.30	4.41	3.48	4.77	66.6	4350	495
	n=36	***n****	*2*	*1*	*28*	*26*	*1*	*0*	*36*	*26*	*5*	*36*	*17*	*4*	*6*	*36*	*36*	*9*	*12*	*36*		*36*
	Gn	**AVR**	4.73	0.83	50.0	5.72	0.19		83.9	94.2	1.30	6617	36.3	1.62	0.14	588	105	5.03	0.61	45.8	n.a.	11419
		MED	4.73	0.83	30.1	2.10	0.19		62.0	82.1	1.23	9447	35.8	0.08	0.13	429	105	0.70	0.13	4.59	n.a.	17770
		GM	0.92	0.83	32.4	2.20	0.19		49.2	56.2	1.26	3902	33.2	0.23	0.13	340	46.9	0.98	0.21	6.12	n.a.	3131
		MIN	0.09	0.83	9.27	0.39	0.19		5.09	5.39	0.84	500	15.2	0.07	0.08	6.90	6.73	0.35	0.04	0.25	n.a.	139
		MAX	9.38	0.83	348	74.1	0.19		344	356	1.69	12720	88.6	6.23	0.20	1313	259	40.1	3.52	210	n.a.	31222
Median detection limits			*0.30*	*2.00*	*1.50*	*5.00*	*0.09*	*0.40*	*3.00*	*15.0*	*0.50*	*0.10*	*0.80*	*0.04*	*0.60*	*0.40*	*2.00*	*0.03*	*0.03*	*0.03*	*0.20*	*0.03*

Note. GM - geometric mean, n - number of analyses, n* - number of analyses above detection limit, n.a. - not analysed as macrocomponent, blank – below detection limit.

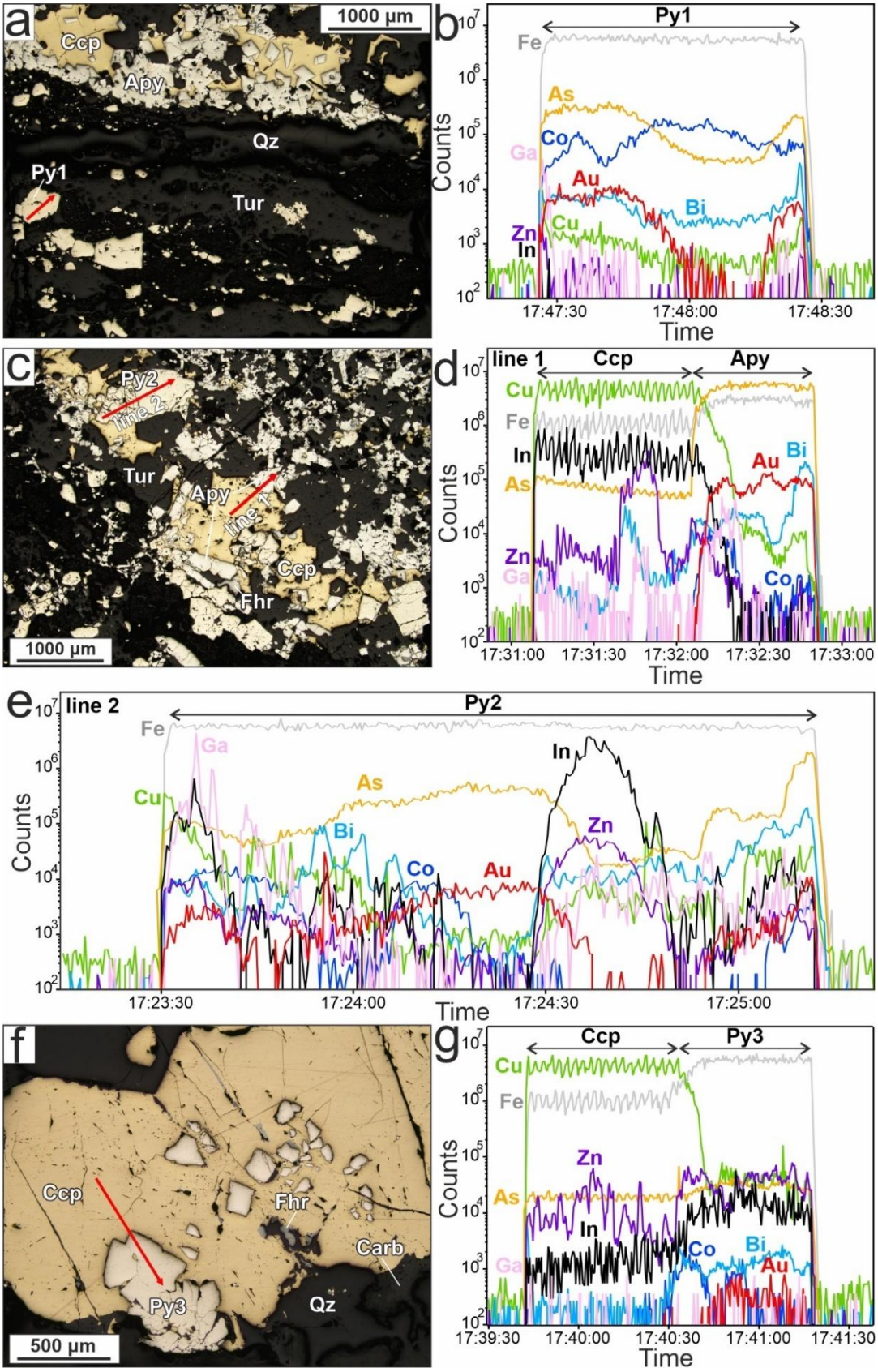


Fig. 6. Time-resolved LA-ICP-MS spectra showing the trace elements distribution in three types of pyrite and other sulfides coexisted in one sample № 20Dr85. **a, c, f** Microphotographs with the outlined profiles at LA-ICP-MS spectra on **b, d, e, f**.

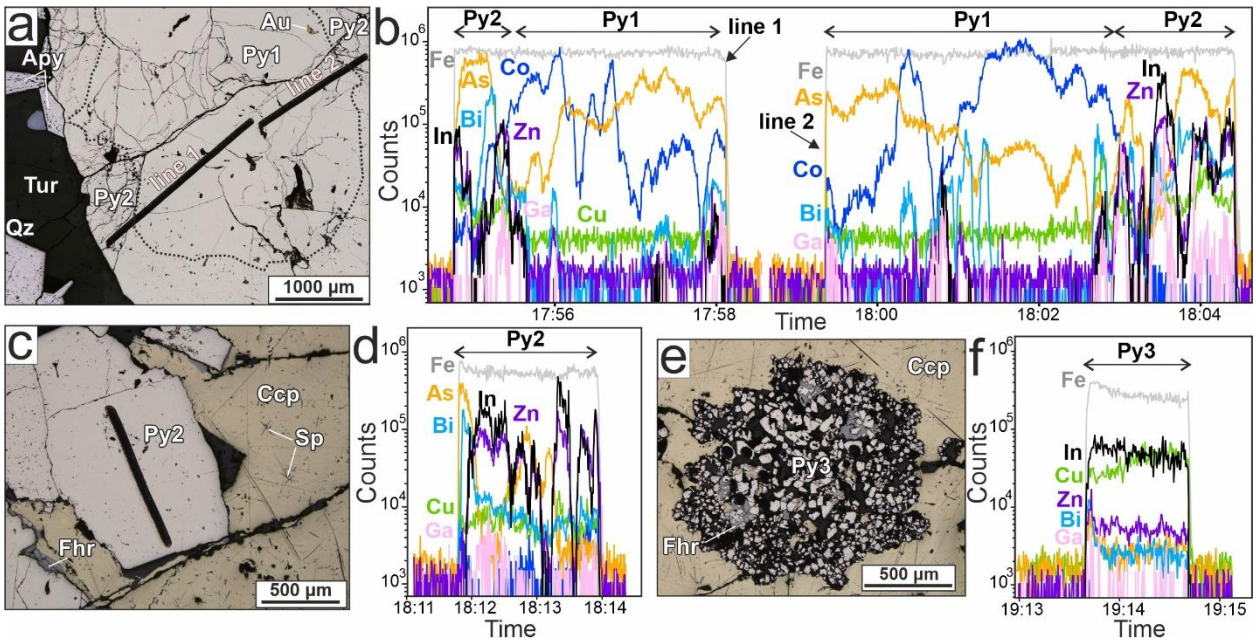


Fig. 7. Time-resolved LA-ICP-MS spectra showing the trace elements distribution in three types of pyrite coexisted in one sample № 20Vd89. **a, c, e** Microphotographs with the ablated profiles and spots at the LA-ICP-MS spectra on b, d, f. **a-b** Profiles through the intergrown Py1 and Py2 with the outlined contact between them.

Arsenopyrite

Arsenopyrite was studied only in samples from the Darasun deposit. According to the EPMA data (Supplementary table S2), arsenopyrite displays a relatively homogeneous composition with As/S ratio (in at.%) ranging from 0.83 to 0.89 and As negatively correlating with S (R^2=0.66). The studied grains of arsenopyrite are generally homogeneous and inclusions-free under BSE, even though there is a patch with oscillatory zoning and directional fine-scale galena inclusions occurring in arsenopyrite near its contact with galena in one sample. Arsenopyrite is enriched in Au, Sb and Te compared to the associated pyrite (Figs. 6, 8) and contains up to (ppm): 259 Au, 377 Sb and 758 Te along with other minor components (Supplementary table S4).

The LA-ICP-MS mapping revealed a trace element zonation within the arsenopyrite grains (Fig. 8). Zones of Au enrichment in arsenopyrite coincides with the zones of Sb depletion and vice versa. The similar to Sb patch enrichment of arsenopyrite is observed for Te at the distributional map. Other elements can both overlap and enrich different zones, mostly confined to the grain contacts. A positive correlation is observed between Pb, Bi, Ag, Cu, and Zn in arsenopyrite. Cobalt enriches only one zone in this map, which coincides with zone of Te and Sb enrichment (Fig. 8).

Arsenopyrite containing the highest values of Au (up to 259 ppm) is associated with Py2 which also has an elevated, but not the highest content of Au (up to 21.9 ppm, sample 224Dr85(1)). For comparison, arsenopyrite with the lowest median Au content (11.8 ppm) from the sample shv80 occurs along with Py2 exhibiting median Au content 0.63 ppm, which is higher than Au median level for this type (Fig. 6). However, based on our data, there is positive correlation (R^2=0.50) between median Au contents

in pyrite and arsenopyrite from the same vein. Nickel in arsenopyrite in turn shows a positive correlation with Co (R^2=0.46) and a weak negative correlation with Mo (R^2=0.33). Copper correlates positively with Zn (R^2=0.39). Silver, Bi and Pb positively correlate with each other in arsenopyrite (R^2>0.93).

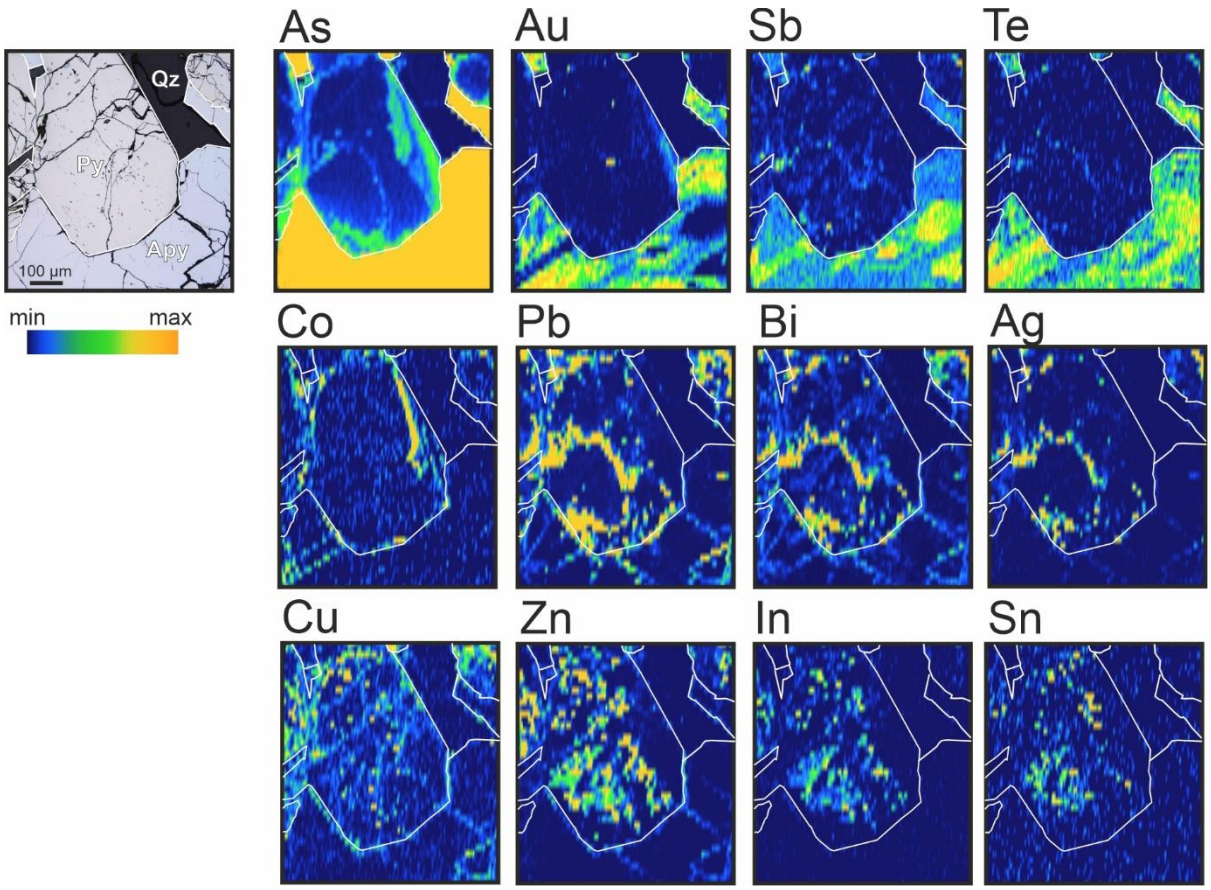
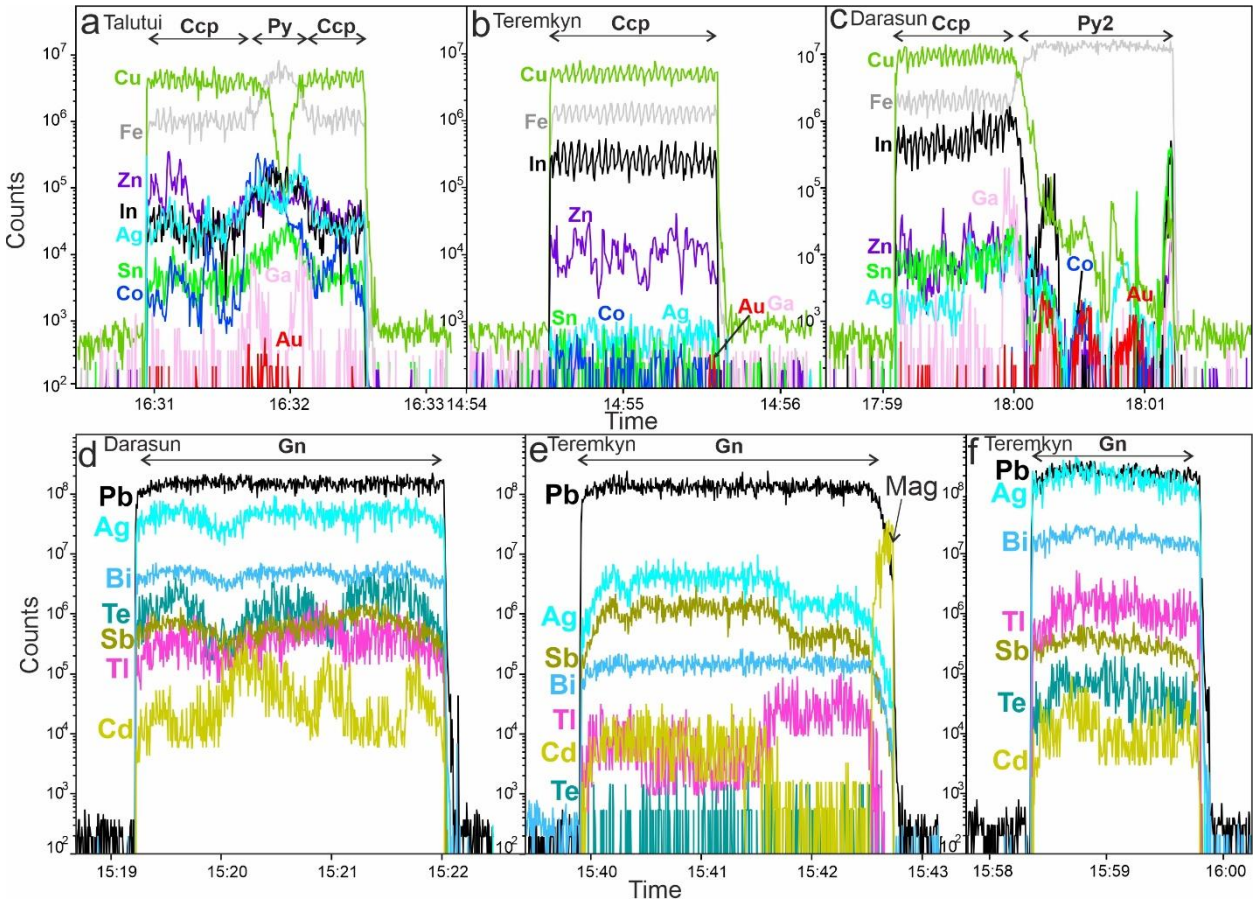


Fig. 8. The LA-ICP-MS maps of trace element distribution in pyrite-arsenopyrite intergrowth in sample № 6Vd-89 from the Darasun deposit.

Chalcopyrite

Chalcopyrite is a main carrier for Zn, Ga, In, and Sn among the studied sulfides (except sphalerite). It also contains Ag, Au and other trace elements as the minor components. Trace element distribution in chalcopyrite varies between the three deposits. The median concentrations of Co and Ni decrease, whereas Au, Sb, and Pb increase in chalcopyrite from Talatui to Teremkyn and to Darasun deposit (Table 1). The Teremkyn chalcopyrite is depleted in Zn, Ag, Ga, Sn, Cd, Te, and Tl, but enriched in In, Pb, and Bi relative to chalcopyrite from the other deposits (Table 1). The Talatui chalcopyrite is characterized by the lowest In and highest Zn contents with the median Zn/In=105. In the Teremkyn and Darasun deposits, the median Zn/In ratios in chalcopyrite are 8.4 and 12, respectively, which is also observed in changing of their signal intensities (Fig. S1). At Talatui, chalcopyrite from Zone 2 is enriched in Ni, Zn, Ag, and Cd, relative to chalcopyrite from Zone 3, similar to pyrite.

The time-resolved LA-ICP-MS profiles reveal systematic differences in trace element residence in chalcopyrite at three deposits. Zinc consistently demonstrates spiked signals, indicating the occurrence of sphalerite micro-inclusions, observed under a petrographic microscope. Indium, in contrast, shows a smooth, homogeneous signal, consistent with incorporation into the chalcopyrite lattice, substituting for Cu or Fe. Silver shows no correlation with Zn and displays its own spiked pattern, suggesting that Ag resides in separate Ag-bearing mineral phases (e.g., argentite or Ag-sulfosalts). Gallium and In show a negative correlation in both Talatui and Darasun chalcopyrite, with R^2 values of 0.62 and 0.25, respectively (Fig. 9a), indicating that Ga-rich domains are In-poor and vice versa. Gallium and Sn display a positive correlation that is remarkably strong at Talatui (R^2=0.81), but weak in Darasun (R^2=0.35), reflecting the tight coupling of Ga and Sn (Fig. 9b). Tin exhibits dual behavior. In Talatui chalcopyrite Sn correlates with Zn, which is observed both at the LA-ICP-MS time-resolved spectra (Fig. S1) and at binary diagram (Fig. 9c). Although, the data on Darasun chalcopyrite demonstrates no correlation between Sn and Zn (Fig. 9c). Cobalt enriches the Talatui chalcopyrite heterogeneously, positively correlating with Ag (R^2=0.69). In the Darasun deposit chalcopyrite, Co content significantly decreases towards the means below detection limit (Fig. S1).



Supplementary Fig. S1. Representative time-resolved LA-ICP-MS spectra of profiles through chalcopyrite (+ coexisted pyrite) from the three deposits **(a-c),** and in galena from the Darasun **(d)** and Teremkyn **(e, f)** deposits.

Galena

Trace element distribution in galena was compared for two deposits – Teremkyn and Darasun. Galena in both deposits is one of the principal sulfides hosting Ag, Sb, Te, Bi, Tl, Cd, and Se (Table 1). The median ranges of trace elements concentrations in galena from both deposits generally display similarities (Table 1; Fig. 9). However, dataset for the Darasun galena is more continuous than for Teremkyn (Fig. 9). In both deposits, Ag shows a strong positive correlation with Bi+Sb in galena (R^2=0.9 for Teremkyn and R^2=0.94 for Darasun; Fig. 9d), consistent with coupled substitution ($Ag^+ + Bi^{3+}/Sb^{3+} \leftrightarrow 2Pb^{2+}$). Thallium and Ag show contrasting relationships in galena from the two deposits. At the Darasun deposit, Tl and Ag correlate positively with R^2=0.71 (Fig. 9e), and their LA-ICP-MS signals at profiles vary together (Fig. S1). In one Teremkyn sample (249T82) galena exhibits an inverse Tl-Ag relationship in the time-resolved signal (Fig. S1) and within the resulting data, but this is an exception and is not representative of the deposit overall (R^2=0.14) (Fig. 9e). In Teremkyn, galena is enriched in Se and Te at higher extent than galena in Darasun (Table 1). Tellurium correlates strongly with Bi+Sb at Teremkyn (R^2=0.73), but not at Darasun (R^2=0.01) (Fig. 9f). In Darasun, some analyses follow the Teremkyn trend, whereas many others show high Bi+Sb at low Te (Fig. 9f). The trace elements are mostly distributed homogeneously within the galena grains at the time-resolved LA-ICP-MS spectra. However, some LA-ICP-MS spectra reveal a zonation with wave-like distribution the trace elements or an enrichment of the specific zones in galena (Fig. S1).

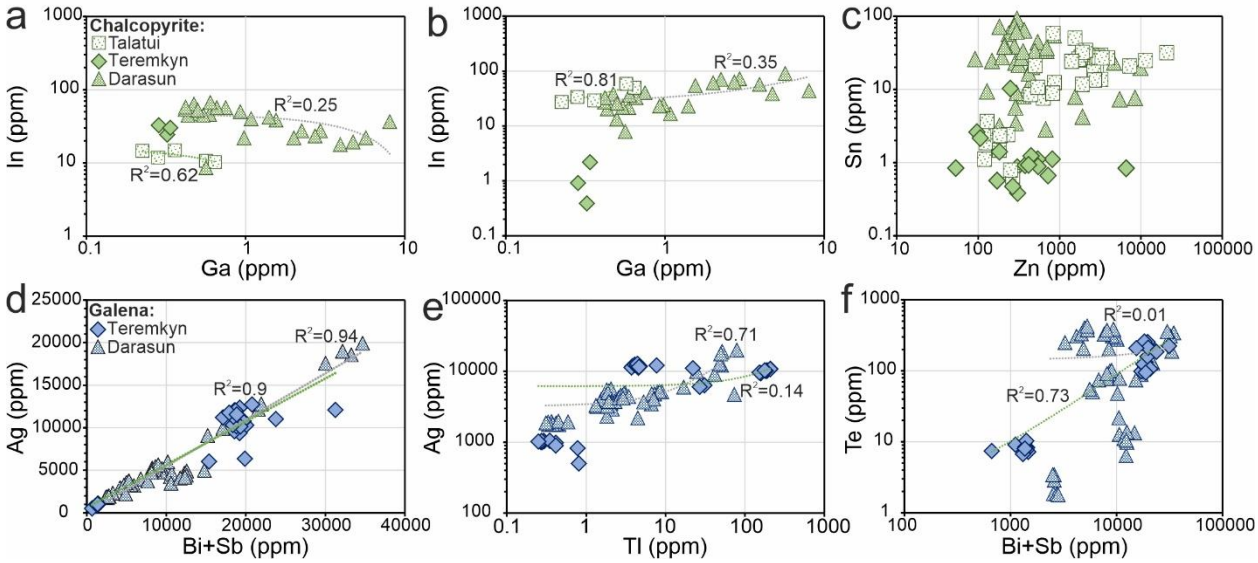


Fig. 9. Binary diagrams of trace elements variations in chalcopyrite (a-c) and galena (d-f). Note a logarithmic scale everywhere except d.

Other sulfides

Sulfosalts (cosalite and galenobismutite) are exceptionally enriched in Ag up to 2.5 wt. % and constantly host Au, In, and Te (Supplementary table S4). Galenobismutite is more enriched in Ag, Cd, In,

514 and Tl, than cosalite. A positive correlation is observed between Ag-Pb (R^2=0.68), Ag-Bi (R^2=0.52), and
515 Ag-Te (R^2=0.48). Indium positively correlates with Cu in sulfosalts from the Teremkyn deposit (R^2=0.76).
516 Fahlore (tetrahedrite) was studied by LA-ICP-MS only in one sample from the Teremkyn deposit, also
517 comprising galena and chalcopyrite. Tetrahedrite consistently contains In, Co, Cd, and Hg, which are
518 distributed heterogeneously. In contrast, the major components (Cu, Zn, As, Ag, and Sb) show
519 homogeneous distribution in the LA-ICP-MS time-resolved spectra, despite minor tiny zonation visible in
520 BSE and EPMA analyses (Supplementary table S2). Trace element concentrations are also investigated in
521 sphalerite from the Teremkyn deposit. Sphalerite shows extreme enrichment in In (104-418 ppm), Ga (0.88-
522 9.57 ppm) and Cd (2717-9150 ppm) and also hosts Co, Cu, As, Ag, Sb, Hg, Pb, and Pb (Supplementary
523 table S4).
524
525 **Sulfur isotope composition of sulfides and sulfates**
526 Sulfides from the Darasun deposit show a bimodal distribution of $\delta^{34}S$ values, with an overall
527 median of –1.0±2.1‰ (n=77) and two well-defined modes at –1.5‰ and at +0.8‰ (Fig. 10a). Both
528 populations are dominated by pyrite, arsenopyrite, and chalcopyrite. Galena has the lightest sulfur isotope
529 composition among the analysed sulfides, whereas sphalerite has the heaviest values, and chalcopyrite
530 displays the broadest range (Supplementary table S6).
531 Sulfides from Talatui and Teremkyn have narrower distributions, with median $\delta^{34}S$ values of
532 0±1.4‰ (n=27) and –1.1±1.1‰ (n=20), respectively (Fig. 10b, c). At Talatui, sulfides from the Zone 2 are
533 isotopically heavier and more variable than those from Zone 3. Pyrite ranges from –0.4 to +1.6‰ and
534 chalcopyrite from –2.5 to +1.5‰ in the Zone 2, compared with –1.8 to +0.6‰ for pyrite and –2.1 to +0.4‰
535 for chalcopyrite in the Zone 3 (Supplementary table S6). Coexisting pyrite is consistently enriched in
536 heavier ^{34}S isotope relative to chalcopyrite, with $\Delta^{34}S = \delta^{34}S_{pyrite} - \delta^{34}S_{chalcopyrite}$ of 1.3‰ on average and up
537 to 2.9‰, corresponding to apparent equilibrium temperatures of 20–640 ºC and with median 517 ºC
538 (Ohmoto and Rye 1979; Li and Liu 2006).
539 Teremkyn sulfides are predominately characterized by negative $\delta^{34}S$ values, although the
540 compositions vary among veins. Only one pyrite-chalcopyrite pair was analysed, yielding $\Delta^{34}S_{Py\text{-}Ccp}$=0.4‰.
541 In sample 1010T, coexisting pyrite and sphalerite differ by 2‰. Apparent temperatures calculated for three
542 coexisting sulfide pairs, based on formulas from (Ohmoto and Rye 1979; Li and Liu 2006), range from 114
543 to 602 ºC.
544 At Darasun, the spatial distribution of $\delta^{34}S$ values is heterogeneous. Median positive values occur
545 near the outer margin of the anhydrite-rich zone, whereas median values become negative both within and
546 farther beyond this domain (Fig. 11). Positive $\delta^{34}S$ values occur in pyrite, arsenopyrite, chalcopyrite, and
547 sphalerite, but were not observed in galena (Supplementary table S6). Three positive $\delta^{34}S$ values in pyrite
548 were recorded within the anhydrite-rich zone in previously published data (Grinenko et al. 2004), whereas
549 four additional positive values in pyrite, chalcopyrite and arsenopyrite occur in the Udachnaya vein based
550 on the present study and Prokofiev et al. (2000). Anhydrite and gypsum also occur outside the main sulfate-

rich zone. Rare anhydrite grains were found in the waste dumps of the South-West mine, and gypsum occurs in the Udachnaya vein (Fig. 11). The Udachnaya vein displays the largest intra-vein sulfur isotope variability with $\delta^{34}S$ ranging from –3.8 to +2.7‰ with median +1.4‰ (Supplementary table S6).

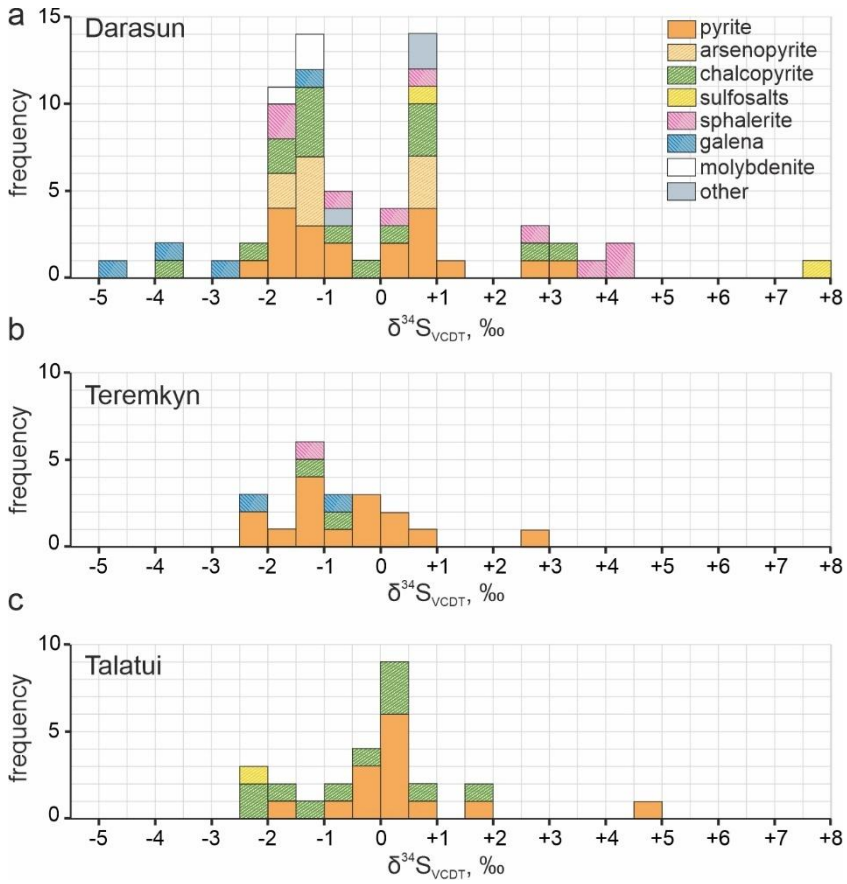


Fig. 10. Histograms of $\delta^{34}S$ values distribution in sulfides from (a) – Darasun, (b) – Teremkyn, and (c) – Talatui deposits, based on our and literature data (Grinenko et al. 2004; Prokofiev et al. 2000; Prokofiev et al. 2007). Other sulfides: fahlore (+0.8‰) and pyrrhotite (+0.7‰).

Sulfur isotope composition has been studied in two samples with sulfates (anhydrite and gypsum) from the Darasun deposit. Anhydrite and gypsum exhibit $\delta^{34}S$ values 14.5 and 15.2, respectively, and the latter is associated with chalcopyrite with $\delta^{34}S$=–3.8‰ (Supplementary table S6). Our new data consistent with the general range of $\delta^{34}S$ values in sulfates at the Darasun deposit from 9.6 to 15.8 ‰ (Grinenko et al. 2004). For 13 sulfide-sulfate pairs, including our and Grinenko et al. (2004) data (Supplementary table S6), the apparent equilibrium temperature was calculated based on (Ohmoto and Rye 1979; Ohmoto 1972; Li and Liu 2006). It comprises the range from 308 to 469 ºC with the median value 397 ºC. Three pairs with $\delta^{34}S$-positive sulfides from Grinenko et al. (2004) correspond to the higher-temperature range from 463 to 548ºC and were used separately for interpretation. The temperature tends to decrease radially outward from the central position. The lowest temperature was obtained for the gypsum – chalcopyrite pair in the Udachnaya vein.

Twenty-five sulfide-sulfide pairs were evaluated in the studied samples, and the $\Delta_{Py\text{-}Ccp}$ value positively correlates with $\Delta_{Py\text{-}Apy}$ value measured in the same samples (R^2=0.85). The pyrite-chalcopyrite pairs have $\Delta^{34}S_{Py\text{-}Ccp}$ values of 0.1–0.9‰ (median 0.5‰), whereas pyrite-arsenopyrite pairs range from 0.2 to 1.5‰ (median 0.7‰). Arsenopyrite is generally isotopically closer to coexisting chalcopyrite than to pyrite. The $\Delta^{34}S_{Apy\text{-}Ccp}$ varies from negative -0.6 to positive +0.3. The temperatures calculated from ten sulfide pairs range from 20 to 640 ºC, with a median of 348 ºC.

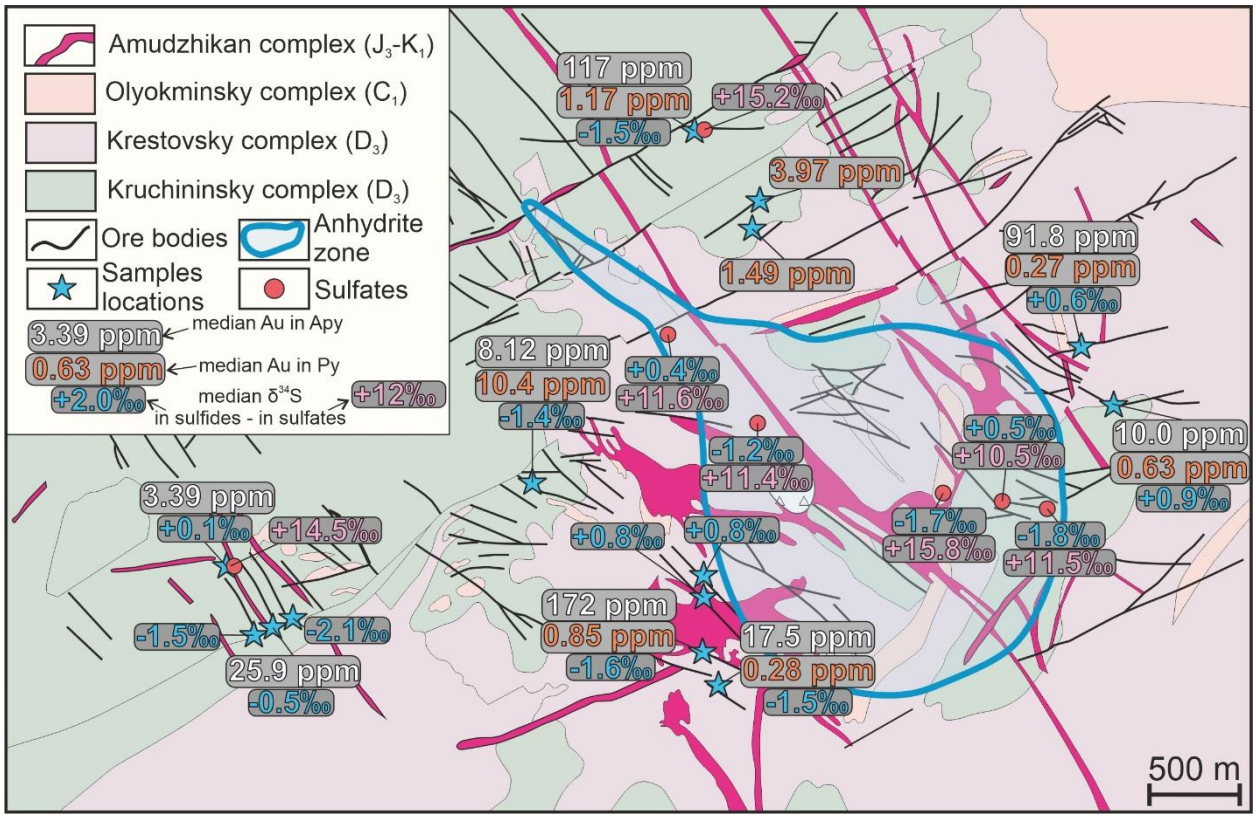


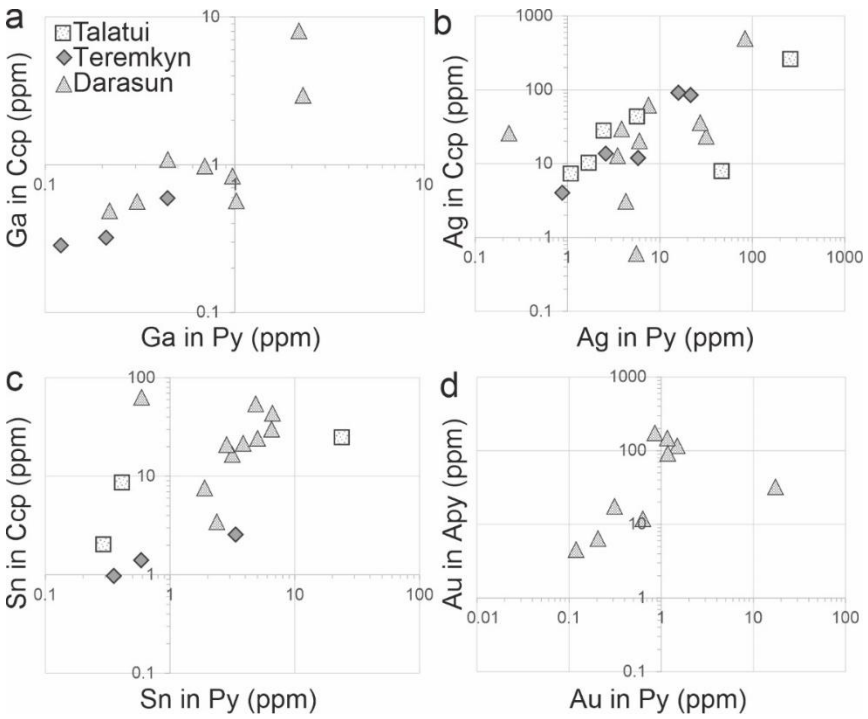
Fig. 11. Geological scheme of the Darasun deposit showing the distribution of the median $\delta^{34}S$ values in sulfides and sulfates (data from this work, from Prokofiev et al. (2000, 2007) and from Grinenko et al. (2004)), as well as median Au content in pyrite and arsenopyrite from the studied samples. The contour of the anhydrite-rich zone is taken from Stolyarov (1980).

Discussion

Paragenetic control of trace elements distribution

The Darasun ore field is considered as a single, large magmatic-hydrothermal system, developed vectorially from ore-forming quartz syenite Amudzhikan intrusion, starting from the close-to-source Talatui deposit, through the intermediate Teremkyn, to the peripheral Darasun deposit (Prokofiev et al. 2010b). Along this vector, the number and diversity of paragenetic mineral associations increase, reflecting the progressive changes in the fluid chemistry and in the physicochemical conditions (Prokofiev et al. 2010b). The pyrite-chalcopyrite and pyrite-arsenopyrite pairs prove to be the most counterbalanced in terms of distribution of trace elements (Fig. S2). The concentrations of Ga, Ag, and Sn in pyrite and chalcopyrite

coexisted with each other are, in general, positively correlated on the binary diagrams (Fig. S2). This observation may confirm the prediction that trace element contents in co-crystallized sulfides should co-vary consistently, which indicates variations in these element concentrations in the ore-bearing fluid (George et al. 2016; Vikentyev 2015).



Supplementary Fig. S2. Co-variations of the median concentrations of Ga, Ag, Sn and Au in (a-c) – pyrite and chalcopyrite, (d) – pyrite-arsenopyrite coexisted in the same sample.

At the Darasun and Teremkyn deposits, successive stages of sulfide formation overlap each other, and this overlap is directly imprinted on the trace element distribution within and between the sulfides. The Talatui ores, by contrast, comprise only two distinct associations: chalcopyrite-dominated (Zone 2) and pyrite-dominated (Zone 3). Pyrite and chalcopyrite from Zone 2 (mod.% Ccp>Py) are enriched in Ni, Zn, Ag, Cd, and Tl, but depleted in Se, In, and Sb, relative to Zone 3 (mod.% Py>Ccp). Pyrite from Zone 3, additionally, shows higher Cu contents, most likely because of the low modal proportion of chalcopyrite leaves Cu without dedicated host and forces it into pyrite. According to LA-ICP-MS time-resolved spectra (Figs. 6, 7), Cu in pyrite occurs in both forms: as solid solution and nano-sized Cu minerals, similarly to the other deposits (Chouinard et al. 2005; Sung et al. 2009; Augustin and Gaboury 2019; Yang and Sun 2023).

Mineral paragenesis has the first-order control on trace element partitioning in most hydrothermal systems (Huston et al. 1995; Cook et al. 2009, 2011, 2016; Vikentyev 2015; George et al. 2016, 2018). At Teremkyn, the appearance and modal increase of sphalerite, galena, and sulfosalts drive strong depletion of Zn, Ga, Se, Ag, Cd, and Te in coexisting pyrite and chalcopyrite, as these elements were preferentially incorporated into the newly formed phases. This behavior is quantitatively consistent with the element

partitioning established for co-crystallized sphalerite-galena-chalcopyrite assemblages, where Zn, Cd, Ga, and In favor sphalerite, and Ag, Tl, Se, Te, and Sb strongly sequestered by galena and sulfosalts (Cook et al. 2009; George et al. 2016; Li et al. 2022; Lan et al. 2026; Soulamidis et al. 2026).

The absence of Bi and Pb depletion in the Teremkyn pyrite and chalcopyrite, despite the abundance of galena and Bi-sulfosalts, indicates that their distribution was not governed by paragenesis. More likely, contents of Bi and Pb in the fluid increased and were controlled by geochemical gradient. Their relative depletion in the Darasun deposit may be attributed to the formation of abundant Bi-Pb and Bi-Te discrete phases. This is consistent with liquid Bi collector model (Douglas 2000; Frost et al. 2001; Ciobanu et al. 2009; Tooth et al. 2011; Vikent'eva et al. 2018; Tyukova et al. 2025) in which Bi-rich melts nucleate independently below ~271 ºC, scavenge Au and Ag, and crystallize as discrete Bi-sulfosalts and tellurides rather than as trace components of pyrite and chalcopyrite. Analogous Bi-Pb decoupling is reported from the Stormont deposit, where the Ag-Au association is controlled by Pb-Bi melts (Cockerton and Tomkins 2012; Cano et al. 2025).

Fluid-controlled geochemical gradient

Concentrations of Co and W in sulfides decrease, for the most part, systematically from the Talatui deposit towards the Darasun deposit, whereas Sb, Sn, and Au increase. These elements evolve primarily as a function of changes in redox conditions, fluid cooling and fractionation, rather than of the local mineral assemblage. The only exception is chalcopyrite, where Sn is depleted at Teremkyn, while W content, in contrast to other sulfides, increases towards the Darasun deposit. Nickel content in chalcopyrite and galena also increases peripherally, whereas Ni in pyrite shows maximum at the Teremkyn deposit and minimum at the Darasun deposit.

Elevated Co in pyrite is long-established evidence for high-temperature, magmatically dominated ore-bearing fluids (Bralia et al. 1979; Bajwah et al. 1987; Belousov et al. 2016; Feng et al. 2020). Experimental study shows that solubility of Co in chloride complexes grows with temperature (Migdisov et al. 2011). Its center-to-periphery decrease is very typical of porphyry systems (Sykora et al. 2018; Xiao et al. 2023), as well as observed within the Darasun ore field. Exceptionally high Co/Ni ratio in the Talatui pyrite (Co/Ni=10) is well corresponding to its high-temperature primarily hydrothermal origin and by proximity to the fluid source. The elevated Ni content and low Co/Ni in pyrite at Teremkyn was attributed to the derivation of Ni from the host Ni-rich gabbro of the Kruchinsky complex (Prokofiev et al. 2023). The same explanation was suggested for Co enrichment in pyrite from a mafic dyke at the Linglong (Jiaodong) gold deposit (Wang et al. 2024). However, Talatui is also hosted by the same Kruchinsky gabbro and pyrite there is not enriched in Ni. The more likely control is fluid-rock interaction intensity. At Teremkyn, mixing with meteoric water is indicated by tourmaline O- and B-isotope data (Prokofiev et al. 2012; Baksheev et al. 2015). The resulting lower-temperature, externally buffered fluids were capable of leaching Ni, while Co remained undersaturated. This hypothesis, however, requires testing against alteration intensity and Ni concentrations in host-rock silicates and stands in contradiction with the gradual center-to-periphery depletion in Ni of chalcopyrite.

Tungsten behaves as a proximal, high-temperature element in exactly the same way as Co in intrusion-related systems (Thompson and Newberry 2000; Hart et al. 2002; Hart 2007). Conversely, the peripheral enrichment in Sb and Au reproduces the classic granite-related magmatic-hydrothermal systems (Hart 2007; Soulamidis et al. 2026), as well as epithermal-peripheral halo signature (Sykora et al. 2018), in which As-Sb-Au are carried furthest from the intrusive source and are incorporated into pyrite as coupled As-Au substitutions at low temperatures (Reich et al. 2005). Similar trends of As-Au positive correlations are observed for the Teremkyn pyrite and for the Darasun Py2 and Py3, and are absent for the Talatui pyrite and Darasun Py1 (Fig. 5a). Experimental reconstruction of conditions closed to the Darasun deposits (at 350 and 490 ºC, and at salinity 0–35 wt. % NaCl) suggests that at Talatui with low As content, Au was stabilized because of high-temperatures and high-NaCl content in fluid (Prokofiev et al. 2022). The similar conditions can be proposed for Py1 at the Darasun deposit. Under certain conditions, particularly at relatively low salinity and temperature, and primarily in the Carlin-type deposits, gold incorporation into pyrite as a solid solution strongly depends on the arsenic content (Reich et al. 2005; Cline et al. 2005; Vikentiev et al. 2019; Prokofiev et al. 2022). However, this control may not be universal. Recent studies of the natural and experimental pyrites indicate that the concentration of As, its speciation, T-P-compositional parameters and redox state of the system do not affect the state of "invisible" Au in pyrites for most gold deposits (Kovalchuk et al. 2019; Kovalchuk et al. 2024).

Antimony and Au are negatively correlated within arsenopyrite grains, enriching the separate zones (Fig. 8), even though concentrations of both these elements in pyrite, galena, and chalcopyrite increase towards the Darasun deposit. Anticorrelation between Sb and Au is very typical of arsenopyrite (Kojonen and Johanson 1999; Sidorova et al. 2025; Li et al. 2026). Although, interrelationships between Sb and Au in arsenopyrite do not follow the general rule (Cook et al. 2013; Li et al. 2019), it is more likely, that the reasons for Au-Sb anticorrelations are related to crystallography, and elevated concentrations of Sb in fluid restrict Au solubility in arsenopyrite, as it was proposed in Li et al. (2019) and Li et al. (2026).

The concentrations of the mineral-controlled elements in pyrite also tend to increase (Cu, Zn, In and Ag) or decrease (Ga, Se, Cd, and Te) when moving from Talatui towards Darasun with pronounced depletion in Teremkyn. Increase in content of Cu and Zn may be a result of higher ability of these elements to be transported in chloride complexes at lower temperatures (Zhong et al. 2015). The peripheral Se-Te decrease is consistent with the systematics of Keith et al. (2018), who showed that Se and Te contents of hydrothermal pyrite are governed by temperature, fS_2 and fTe_2 and decrease sharply as magmatic volatile input wanes. Comparable Se and Te peripheral decrease was demonstrated in vent-chimney zone refining sequences of the Yaman-Kasy VHMS deposit (Maslennikov et al. 2009).

Three types of pyrite

Multigeneration pyrite has proved to be one of the most unequivocal indicators of fluid evolution in ore systems worldwide (Large et al. 2009; Sykora et al. 2018; Zhang et al. 2024). The three pyrite types identified at Darasun record a progressive evolution of the hydrothermal system, consistent with the regional geochemical trends from Talatui to Darasun.

Pyrite 1 retains a high-temperature Co-Ni signature comparable to the close-to-source Talatui pyrite (however at lower Ni and Co/Ni) and is largely depleted in other elements, indicating the least modified generation and best representing the earliest composition of the fluid. Pyrite 2 hosts abundant micro-inclusions of sphalerite and sulfosalts, producing marked enrichment in precisely those elements depleted in Py1. Its complex zoning, with As-Au correlations and with ring-like Pb-Bi-Ag zones (Fig. 8), displays coherent behavior of these elements during pyrite formation at the most Au-productive stage of Darasun ore field deposits. Elevated As/Co in Py2 (up to 20000) may indicate precipitation from a vapor-rich fluid, because As preferentially partitions into the vapor phase, whereas Co remains mainly in the liquid phase (Tardani et al. 2017; Nestmeyer et al. 2021). This is also supported by decoupling behavior of these elements at LA-ICP-MS maps of Py2 (Fig. 8).

Pyrite 3, in contrast, is not a product of fluid cooling and fractionation but a remobilized or recrystallized pyrite generation. The anomalously high Zn and In (even exceeding coexisting chalcopyrite) and elevated Cu in Py3 is best explained by remobilization of sphalerite or sulfosalts inclusions abundant in Py2 as well as the additional input of these elements from later fluid. The same process is suggested for Py3 relatively homogeneous enrichment in other elements (Pb, Bi, Ag, Sn, Tl) occurring in Py2, likely, as nanoinclusions of distinct minerals, rather than solid solutions. Coupled dissolution-reprecipitation replacement is now recognized as the dominant mechanism of such trace element redistribution in sulfides, producing exactly this pattern of selective enrichment and depletion without general textural distraction (Fougerouse et al. 2016; Wu et al. 2019). Crucially, Py3 is absent at Talatui and Teremkyn, demonstrating that the remobilization event was localized and affected only the Darasun deposit area. The co-existence of all three pyrite types in single samples in Lagunov vein suggests a repeatedly reopened hydrothermal system in this vein.

Sulfur isotopes and origin of sulfates

Sulfides from all three deposits define a narrow, near-zero $\delta^{34}S$ range (Talatui 0‰, Teremkyn –1.1‰, Darasun bimodal with median –1.0‰ and two modes at –1.5‰ and +0.8‰), consistent with a homogeneous large magmatic sulfur reservoir with $\delta^{34}S \approx 0$‰ (Prokofiev et al. 2000, 2010a). At Talatui, high temperatures minimized fractionation, and sulfide $\delta^{34}S$ approached fluid values. Mixing with meteoric water at Teremkyn is supported by isotope studies of tourmaline (Prokofiev et al. 2012; Baksheev et al. 2015) and is likely reflected in the anomalously high Ni content in pyrite. This mixing, together with the progressive cooling, increased sulfur isotope fractionation between sulfides and fluid H_2S, that resulted in negative $\delta^{34}S = –1.1$‰ median values of sulfides. Similar cooling- and mixing-driven $\delta^{34}S$ shifts have been documented in the Cadia alkalic Cu-Au porphyry (Wilson et al. 2007), the Myszków Mo-Cu-W porphyry (Naglik et al. 2025), and the Altar Cu-Au porphyry-epithermal systems (Maydagán et al. 2013).

At the Darasun deposit, tourmaline does not exhibit the same isotope characteristics as at Teremkyn (Prokofiev et al. 2012; Baksheev et al. 2015), suggesting that the magmatic fluid at the Darasun deposit was not significantly diluted by meteoric water during tourmaline crystallization. Nevertheless, evidence for fluid interaction with meteoric water at Darasun comes from O isotope data of carbonates (Prokofiev et

al. 2010a) and from isotopic signatures of the associating quartz and anhydrite (Grinenko et al. 2004). However, meteoric water input alone cannot explain the observed variations within the Darasun deposit. The bimodal distribution of $\delta^{34}S$ values in Darasun sulfides (Fig. 10) coincides spatially with three features: the sulfate-rich zone, the zone of paragenetic change, and includes the Lagunov vein where three pyrite types coexist (Figs. 2, 11).

This sulfate-rich zone is defined by an anhydrite-bearing core with a gypsum cap and overlying argillitic and quartz-sericite alteration (Slolyarov 1980). Although anhydrite is also documented in Talatui as an accessory mineral (Prokofiev et al. 2010b), its paragenetic expression is most pronounced at Darasun. Similar sulfide-anhydrite associations are known in porphyry, epithermal and VMS deposits and are formed under highly oxidizing SO_4-enriched conditions during SO_2 disproportionation (Brathwaite et al. 2001; Field et al. 2005; Maydagán et al. 2013). The coexistence of isotopically heavy sulfates and sulfides with $\Delta \approx 13.6‰$ (for 13 sulfate-sulfide pairs) at the Darasun deposit is compatible with SO_2 disproportionation during cooling below 400ºC (Field et al. 2005). The gypsum cap above an anhydrite dome at Darasun (Slolyarov 1980) reflects retrograde solubility of $CaSO_4$ and was formed by hydration at lower temperatures (Blount and Dickson 1973). Cooling and dissociation of H_2SO_4, derived from SO_2 disproportionation, generated an acidic condensate that leached the host rocks and formed zone of argillitic and quartz-sericite alteration, as proposed for similar interrelationships at porphyry Cu-Mo-Au quartz-sulfide-gold-anhydrite veins in the Thames District, New Zealand (Brathwaite et al. 2001).

The main stage at the Darasun deposit occurred at 200-400 ºC (Prokofiev et al. 2010b) under H_2S-dominated conditions with $\delta^{34}S$ of fluid ($\sum S$) ≈ 0 ‰, yielding sulfides with negative $\delta^{34}S$ values at median –1.5‰, which is consistent with the experimental studies of sulfur isotope fractionation between H_2S and pyrite (Syverson et al. 2015). Sulfate formation was induced at higher SO_4/H_2S ratio and slightly heavier $\delta^{34}S_{\sum S} \approx +1.5‰$ (Fig. 12a). The SO_4/H_2S ratio for 13 sulfate-sulfide pairs ranges from 0.2 to 0.39 (Fig. 12b) and shows no correlation with equilibrium temperatures, indicating that temperature was not the primary control of SO_4/H_2S ratio (Fig. 12c). The homogenization temperatures of 214-247ºC for fluid inclusions in anhydrite from the Darasun deposit (Prokofiev et al. 2010b) are lower than those calculated from sulfides-sulfate pairs (from 308 to 459ºC), whereas fluid inclusions in quartz show partial match (Fig. 12c). This discrepancy is controlled by kinetics rather than disequilibrium. Fluid inclusions capture entrapment during cooling stage, whereas slow exchange kinetics prevent the sulfide-anhydrite pair from re-equilibrium, locking in a temperature closer to the maximum.

The spatial association of sulfates with granodiorite porphyry dykes (Fig. 11) may indicate that dykes acted as heat sources and fluid conduits, locally promoted oxidized conditions favorable for sulfate formation. Apart from deep-seated anhydrite, this domain is also characterized by quartz-tourmaline veins with pyrite, and massive sulfides are scarce there (Timofeyevsky 1972). Away from this domain, cooling and fluid-rock interaction produced a reaction zone where fO_2 decreased and H_2S become more dominant. This zone involves the Lebedev I, Lebedev II and Iskra veins containing sulfides with only positive $\delta^{34}S$ values, and partly the Razvedochnaya, Udachnaya, and Lagunov veins having sulfides with both negative

765 and positive $\delta^{34}S$ values (Supplementary table S6). Unlike $\delta^{34}S$-negative sulfides, sulfide associations with
766 positive $\delta^{34}S$ values are rarely represented by equilibrated pairs (Prokofiev et al. 2000), which argues against
767 simple closed-system fractionation. Instead, it suggests mixing between magmatic reduced sulfur and sulfur
768 derived from partial dissolution or reduction of preexisted sulfates. Sulfates also occur in some lower-
769 temperature peripheral veins (Fig. 11), coexisting with mostly $\delta^{34}S$-negative sulfides and a subordinate
770 sulfide population with slightly positive $\delta^{34}S$ values (Supplementary table S6). Furthermore, according to
771 Grinenko et al. (2004), $\delta^{34}S$-positive pyrite has been found in association with anhydrite in three samples,
772 also characterized by the highest apparent equilibrium temperatures (from 463 to 548ºC) and the lowest
773 SO_4/H_2S ratio (0.07-0.11). These analyses were not taken into account on Fig. 12, as they apparently do not
774 represent equilibrated pairs. The spatial association of the $\delta^{34}S$-positive sulfides with known sulfate
775 occurrences is consistent with late-stage, localized interaction between reduced fluid and the preexisting
776 sulfate minerals (anhydrite or gypsum). Such interaction may have introduced sulfate-derived sulfur into
777 the fluid and promoted precipitation of new $\delta^{34}S$-positive sulfides, however, the available data do not
778 distinguish this process from localized dissolution-reprecipitation or isotopic resetting of preexisted
779 sulfides.
780 The heaviest $\delta^{34}S$ values were documented in the late mineral associations with sphalerite and
781 sulfosalts (Supplementary table S6). In sample 9Vd89-1 from the Iskra vein, pyrite with arsenopyrite and
782 chalcopyrite has $\delta^{34}S$=+0.9‰, whereas pyrite from another part of the same sample with sulfosalt-bearing
783 assemblage has $\delta^{34}S$=+2.7‰ and sulfosalt has $\delta^{34}S$=+7.8‰ (Prokofiev et al. 2000). These late assemblages
784 are commonly associated with light-$\delta^{18}O$ quartz (down to 4.7‰) according to Prokofiev et al. (2000) data.
785 The higher $\delta^{18}O$ values (~ +12‰) likely record an earlier, predominantly magmatic-hydrothermal fluid,
786 whereas the lower values (~ +4.7‰) are consistent with the later mixing with isotopically lighter meteoric
787 water (Prokofiev et al. 2000). A similar inference was made for $\delta^{18}O$ of coexisting quartz with $\delta^{18}O$ between
788 +6.4 and +11.7‰ and anhydrite having $\delta^{18}O$ values from +7.0 to +17.1‰ (Grinenko et al. 2004). The strong
789 inverse correlation between quartz $\delta^{18}O$ and sulfide $\delta^{34}S$ indicates that meteoric-water influx accompanied
790 the final pulse of sulfate-derived sulfur into the reduced fluid and together formed the late mineral
791 assemblages in these veins.
792 The absence of systematic correlation between $\delta^{34}S$ and trace element composition across most
793 sulfides indicates that sulfur isotope fractionation and metal incorporation were decoupled in the Darasun
794 system. At the Darasun deposit, median Au concentrations in pyrite and arsenopyrite do not show any
795 consistency with distribution of two sulfide populations with the contrasting $\delta^{34}S$ values (Fig. 11). The only
796 exception is Ag, which shows a positive covariation with $\delta^{34}S$ across three deposits, (Fig. S3). This
797 decoupling suggests that sulfur isotope variations were controlled by cooling and redox equilibria, whereas
798 trace element distributions were governed by additional factors, including mineral competition and the form
799 of element occurrence in each sulfide. The Ag-$\delta^{34}S$ correlation in chalcopyrite may reflect the fact that both
800 parameters responded to the same cooling and fluid-evolution path. The contrasting behavior of pyrite,

where no such correlation is observed, may point to a different form of Ag occurrence, most likely as micro-inclusions, consistent with LA-ICP-MS mapping and enrichment of remobilized Py3 in Ag.

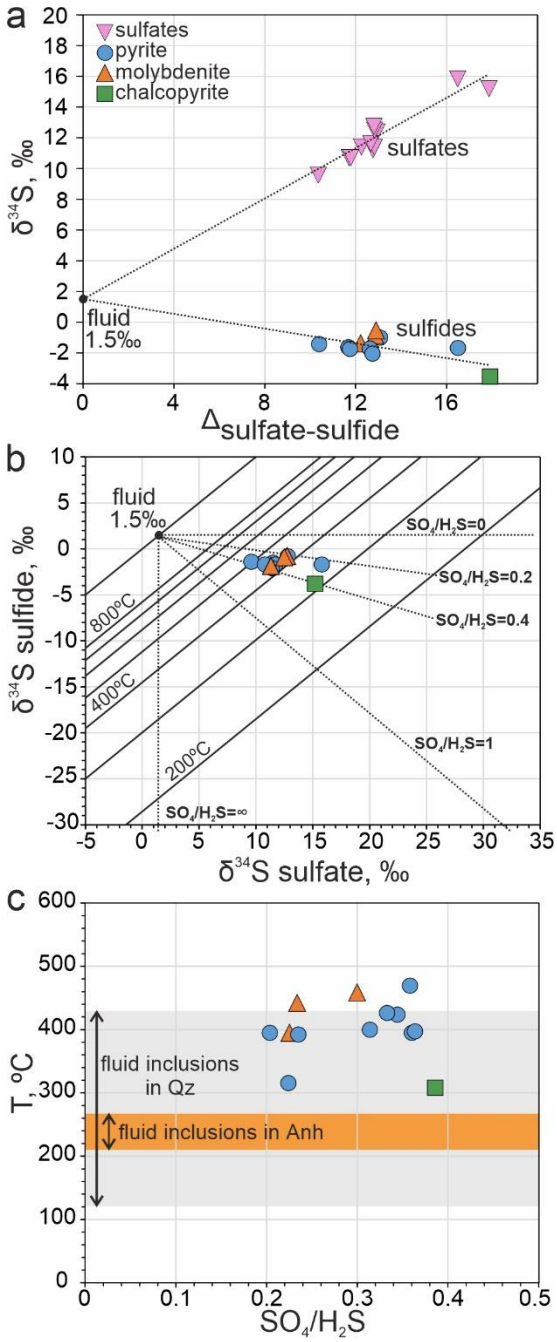
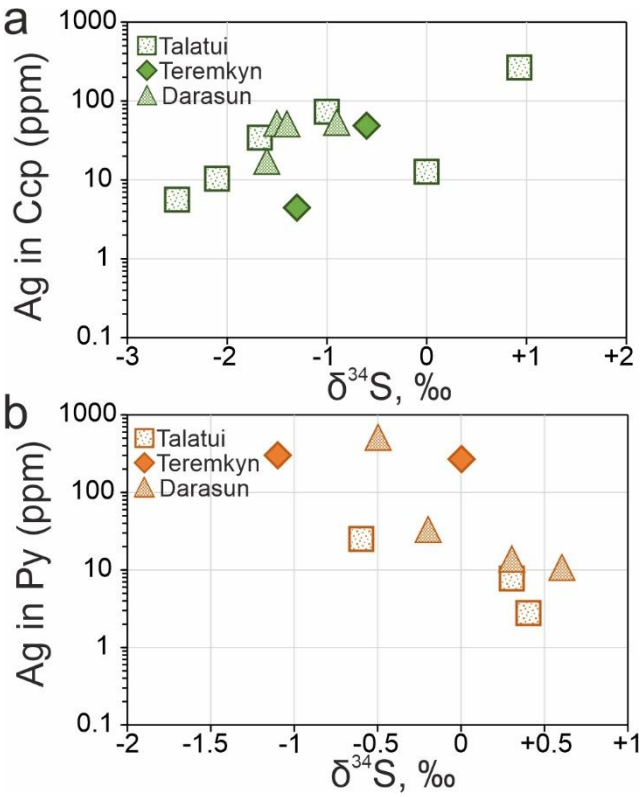


Fig. 12. Sulfur isotope systematics of sulfate-sulfide mineral pairs form the Darasun deposit (our and Grinenko et al., 2004 data). **a** The $\delta^{34}S$ values versus $\Delta_{sulfate\text{-}sulfide}$. The intersection of the two regression lines defines the bulk sulfur isotope composition of the fluid. **b** The $\delta^{34}S$ (sulfide) versus $\delta^{34}S$ (sulfate) diagram with contours of SO_4/H_2S ratio (dashed lines) and isotherms (solid lines). **c** Calculated equilibrium temperatures for sulfate-sulfide pairs plotted against SO_4/H_2S ratio. The horizontal bars show the homogenization temperature range of fluid inclusions in quartz (grey) and anhydrite (orange) from Prokofiev et al. (2010b).



Supplementary Fig. S3. Plot of Ag content versus $\delta^{34}S$ value measured in situ in the same area after polishing. **a** in chalcopyrite. **b** in pyrite from the Darasun goldfield deposits.

Conclusion

The Darasun goldfield evolved through several stages, each with its own geochemical and isotopic signatures. The observed trace element patterns reflect the combined effects of cooling, changing sulfide assemblages, mineral competition, and local redistribution of metals. Two groups of elements are distinguished: fluid-controlled elements (Co, W, Sb, Sn, Au) that follow cooling and fractionation, and mineral-sensitive elements (Cu, Zn, Ag, In, Ga, Cd, Se, Te) that are depleted in pyrite and chalcopyrite as sphalerite, galena and sulfosalts start to precipitate. Three pyrite generations at the Darasun deposit formed during successive stages of this process, with Py3 representing the result of a late metal redistribution event. The sulfur isotope composition of sulfides at the Darasun goldfield was controlled by the interaction between a reduced magmatic-hydrothermal fluid with $\delta^{34}S_{\Sigma S} \approx 0‰$, meteoric water and a sulfate reservoir stored in anhydrite and gypsum. Granitoid porphyry dykes at the Darasun deposit created a radial temperature-redox gradient with anhydrite localized in the hot, relatively oxidized central part of the system. This anhydrite formed early from fluid and acquired heavy ^{34}S which was subsequently transferred to late sulfides (especially sphalerite and sulfosalts) in veins proximal to anhydrite-bearing domains through partial dissolution or reduction.

Supplementary Information

Supplementary table S1. Brief information about the studied samples.

Supplementary table S2. Major elements composition of sulfides from the Darasun deposits measured by EPMA.

Supplementary table S3. Parameters of EPMA analyses.

Supplementary table S4. Trace elements concentrations in sulfides from the Darasun deposits measured by LA-ICP-MS.

Supplementary table S5. The results of the SRM measurements for estimation of accuracy and precision of the LA-ICP-MS analysis.

Supplementary table S6. Sulfur isotope composition of sulfides from the Darasun deposits.

Supplementary Fig. S1. Representative time-resolved LA-ICP-MS spectra of profiles through chalcopyrite (+ coexisted pyrite) from the three deposits (a-c), and in galena from the Darasun (d) and Teremkyn (e, f) deposits.

Supplementary Fig. S2. Co-variations of the median concentrations of Ga, Ag, Sn and Au in (a-c) – pyrite and chalcopyrite, (d) – pyrite-arsenopyrite coexisted in one sample.

Supplementary Fig. S3. Plot of Ag content versus $\delta^{34}S$ value measured in situ in the same area after polishing. a in chalcopyrite. b in pyrite from the Darasun goldfield deposits.

Acknowledgments

The authors would like to thank L.D. Zorina for providing the samples for this research. We are deeply grateful to T.A. Velivetskaya, S.G. Kryazhev, L.P. Nosik and E.V. Kovalchuk for their analytical assistance. We also would like to express our gratitude to M.A. Yudovskaya for her comprehensive support of our research.

Author contributions

Conceptualization: **VB**, **VP.** Investigation: **VB**, **VP, VA, SS.** Data curation: **VB**. Formal Analysis: **VB.** Visualization: **VB.** Writing original draft: **VB**, **VP, IV.** Resources: **VP**. Methodology: **VA, SS.** Funding acquisition: **IV, VP.** Writing review & editing: **VP, IV**.

Funding

This work was financially supported by the Ministry of Science and Higher Education (project no. 13.1902.24.44).

References

Augustin J, Gaboury D (2019) Multi-stage and multi-sourced fluid and gold in the formation of orogenic gold deposits in the world-class Mana district of Burkina Faso–Revealed by LA-ICP-MS analysis of pyrites and arsenopyrites. Ore Geology Reviews 104:495-521.

Bajwah Z, Seccombe P, Offler R (1987) Trace element distribution, Co: Ni ratios and genesis of the Big Cadia iron-copper deposit, New South Wales, Australia. Mineralium Deposita 22:292-300.

Baksheev IA, Trumbull RB, Popov MP, Erokhin YV, Kudryavtseva OE, Yapaskurt VO, Khiller VV, Vovna GM, Kiselev VI (2015) Chemical and boron isotopic composition of tourmaline from the Mariinsky emerald deposit, Central Urals, Russia. Mineralium Deposita 53:565-583.

Belousov I, Large R, Meffre S, Danyushevsky L, Steadman J, Beardsmore T (2016) Pyrite compositions from VHMS and orogenic Au deposits in the Yilgarn Craton, Western Australia: Implications for gold and copper exploration. Ore Geology Reviews 79:474-499.

Blount CW, Dickson FW (1973) Gypsum-anhydrite equilibria in systems $CaSO_4$-H_2O and $CaCO_4$-NaCl-H_2O. American Mineralogist: Journal of Earth and Planetary Materials 58:323-331.

Bralia A, Sabatini G, Troja F (1979) A revaluation of the Co/Ni ratio in pyrite as geochemical tool in ore genesis problems: Evidences from southern Tuscany pyritic deposits. Mineralium Deposita 14:353-374.

Brathwaite R, Simpson M, Faure K, Skinner D (2001) Telescoped porphyry Cu-Mo-Au mineralisation, advanced argillic alteration and quartz-sulphide-gold-anhydrite veins in the Thames District, New Zealand. Mineralium Deposita 36:623-640.

Cano N, María González-Jiménez J, Camprubí A, Proenza JA, González-Partida E (2025) Macro-to nanoscale investigation unlocks gold and silver enrichment by lead-bismuth metallic melts in the Switchback epithermal deposit, southern Mexico. American Mineralogist 110:582-593.

Chernyshev I, Prokof'ev VY, Bortnikov N, Chugaev A, Goltsman YV, Lebedev V, Larionova YO, Zorina L (2014) Age of granodiorite porphyry and beresite from the Darasun gold field, eastern Transbaikal region, Russia. Geology of Ore Deposits 56:1-14.

Chouinard A, Paquette J, Williams-Jones AE (2005) Crystallographic controls on trace-element incorporation in auriferous pyrite from the Pascua epithermal high-sulfidation deposit, Chile–Argentina. The Canadian Mineralogist 43:951-963.

Ciobanu CL, Cook NJ, Pring A, Brugger J, Danyushevsky LV, Shimizu M (2009) 'Invisible gold'in bismuth chalcogenides. Geochimica et Cosmochimica Acta 73:1970-1999.

Cline JS, Hofstra AH, Muntean JL, Tosdal RM, Hickey KA (2005) Carlin-type gold deposits in Nevada: Critical geologic characteristics and viable models. Economic Geology, 100th Anniversary 504-516.

Cockerton AB, Tomkins AG (2012) Insights into the liquid bismuth collector model through analysis of the Bi-Au Stormont skarn prospect, northwest Tasmania. Economic Geology 107:667-682.

Cook N, Ciobanu CL, George L, Zhu Z-Y, Wade B, Ehrig K (2016) Trace element analysis of minerals in magmatic-hydrothermal ores by laser ablation inductively-coupled plasma mass spectrometry: Approaches and opportunities. Minerals 6:111.

Cook NJ, Ciobanu CL, Pring A, Skinner W, Shimizu M, Danyushevsky L, Saini-Eidukat B, Melcher F (2009) Trace and minor elements in sphalerite: A LA-ICPMS study. Geochimica et Cosmochimica Acta 73:4761-4791.

Cook NJ, Ciobanu CL, Danyushevsky LV, Gilbert S (2011) Minor and trace elements in bornite and associated Cu–(Fe)-sulfides: A LA-ICP-MS studyBornite mineral chemistry. Geochimica et Cosmochimica Acta 75:6473-6496.

Cook NJ, Ciobanu CL, Meria D, Silcock D, Wade B (2013) Arsenopyrite-pyrite association in an orogenic gold ore: Tracing mineralization history from textures and trace elements. Economic Geology 108:1273-1283.

Douglas N (2000) The liquid bismuth collector model: an alternative gold deposition mechanism Geological Society of Australia Abstracts. Geological Society of Australia. 59:135.

Feng Y, Zhang Y, Xie Y, Shao Y, Lai C (2020) Pyrite geochemistry and metallogenic implications of Gutaishan Au deposit in Jiangnan Orogen, South China. Ore Geology Reviews 117:103298.

Field C, Zhang L, Dilles J, Rye RO, Reed M (2005) Sulfur and oxygen isotopic record in sulfate and sulfide minerals of early, deep, pre-Main Stage porphyry Cu–Mo and late Main Stage base-metal mineral deposits, Butte district, Montana. Chemical Geology 215:61-93.

Fougerouse D, Micklethwaite S, Tomkins AG, Mei Y, Kilburn M, Guagliardo P, Fisher LA, Halfpenny A, Gee M, Paterson D (2016) Gold remobilisation and formation of high grade ore shoots driven by dissolution-reprecipitation replacement and Ni substitution into auriferous arsenopyrite. Geochimica et Cosmochimica Acta 178:143-159.

Frost BR, Barnes CG, Collins WJ, Arculus RJ, Ellis DJ, Frost CD (2001) A geochemical classification for granitic rocks. Journal of Petrology 42:2033-2048.

George LL, Cook NJ, Ciobanu CL (2016) Partitioning of trace elements in co-crystallized sphalerite–galena–chalcopyrite hydrothermal ores. Ore Geology Reviews 77:97-116.
George LL, Cook NJ, Crowe BB, Ciobanu CL (2018) Trace elements in hydrothermal chalcopyrite. Mineralogical Magazine 82:59-88.
Grinenko V, Ustinov V, Karpukhina V (2004) Evolution of the ore bearing fluid during formation of the Darasun gold base metal deposit Proceedings of the 11th International Conference on Inclusions in Minerals, Aleksandrov, Russia. pp 329-335.
Hart CJ, McCoy DT, Goldfarb RJ, Smith M, Roberts P, Hulstein R, Bakke AA, Bundtzen TK (2002) Geology, exploration, and discovery in the Tintina Gold Province, Alaska and Yukon. Society of Economic Geologists Special Publication 9:241-274.
Hart CJ (2007) Reduced intrusion-related gold systems. Mineral Deposits of Canada: A synthesis of Major deposit types, district metallogeny, the Evolution of geological provinces, and exploration methods: Geological Association of Canada, Mineral Deposits Division, Special Publication 5:95-112.
Huston DL, Sie SH, Suter GF, Cooke DR, Both RA (1995) Trace elements in sulfide minerals from eastern Australian volcanic-hosted massive sulfide deposits; Part I, Proton microprobe analyses of pyrite, chalcopyrite, and sphalerite, and Part II, Selenium levels in pyrite; comparison with delta 34 S values and implications for the source of sulfur in volcanogenic hydrothermal systems. Economic Geology 90:1167-1196.
Kazimirovsky M, Zorina L, Kulikova Z (1993) The evolution of Paleozoic ultramafic and mafic magmatism of the Darasun ore district. Otechestv Geol 9:54-60.
Keith M, Smith DJ, Jenkin GR, Holwell DA, Dye MD (2018) A review of Te and Se systematics in hydrothermal pyrite from precious metal deposits: Insights into ore-forming processes. Ore Geology Reviews 96:269-282.
Kojonen K, Johanson B (1999) Determination of refractory gold distribution by microanalysis, diagnostic leaching and image analysis. Mineralogy and Petrology 67:1-19.
Kovach V, Kotov A, Larin A, Sal'nikova E, Velikoslavinskii S, Yakovleva S, Plotkina YV (2018) Age and boundaries of the Olekma magmatic belt of the Selenga–Stanovoi superterrane (Central Asian Mobile Belt) Doklady Earth Sciences. Springer, pp 1375-1379.
Kovalchuk E, Tagirov B, Vikentyev I, Chareev D, Tyukova E, Nikolsky M, Borisovsky S, Bortnikov N (2019) "Invisible" gold in synthetic and natural arsenopyrite crystals, Vorontsovka Deposit, Northern Urals. Geology of Ore Deposits 61:447-468.
Kovalchuk EV, Tagirov BR, Borisovsky SE, Nickolsky MS, Tyukova EE, Sidorova NV, Komarov VB, Mezhueva AA, Prokofiev VY, Vikentyev IV (2024) Gold and arsenic in pyrite and marcasite: hydrothermal experiment and implications to natural ore-stage sulfides. Minerals 14:170.
Lan K, Zhou Y, Miao Y, Li M, Wu L, Zhou J, Luo K, Li S (2026) A Study of the Trace Element Enrichment Patterns in Sulfides from the Maoping Pb-Zn Deposit, SW China. Minerals 16:130.
Large RR, Danyushevsky L, Hollit C, Maslennikov V, Meffre S, Gilbert S, Bull S, Scott R, Emsbo P, Thomas H (2009) Gold and trace element zonation in pyrite using a laser imaging technique: Implications for the timing of gold in orogenic and Carlin-style sediment-hosted deposits. Economic Geology 104:635-668.
Larin A, Kotov A, Sal'nikova E, Kovach V, Savatenkov V, Velikoslavinskii S, Rizvanova N, Sergeeva N, Skovitina T, Zagornaya NY (2024) Amudzhikan volcano-plutonic association of the eastern part of the West-Stanovoy superterrane (Central Asian orogenic belt): age, sources, and tectonic setting. Petrology 32:502-533.
Li G, Zhao Z, Wei J, Ulrich T (2022) Trace element compositions of galena in an MVT deposit from the Sichuan-Yunnan-Guizhou metallogenic province, SW China: Constraints from LA-ICP-MS spot analysis and elemental mapping. Ore Geology Reviews 150:105123.
Li W, Cook NJ, Xie G-Q, Mao J-W, Ciobanu CL, Li J-W, Zhang Z-Y (2019) Textures and trace element signatures of pyrite and arsenopyrite from the Gutaishan Au–Sb deposit, South China. Mineralium Deposita 54:591-610.
Li X, Li H, Hou Y, Wang R, Ghaderi M, Zhou Z, Wen C, Chen S (2026) Fluid source and evolutionary processes of the Jinkeng and Huanggou gold deposits, southwestern Hunan, South China: Constraints from pyrite and arsenopyrite chemistry and quartz HO isotopes. Geochemistry:126417.
Li Y, Liu J (2006) Calculation of sulfur isotope fractionation in sulfides. Geochimica et Cosmochimica Acta 70:1789-1795.

Maslennikov V, Maslennikova S, Large R, Danyushevsky L (2009) Study of trace element zonation in vent chimneys from the Silurian Yaman-Kasy volcanic-hosted massive sulfide deposit (Southern Urals, Russia) using laser ablation-inductively coupled plasma mass spectrometry (LA-ICP-MS). Economic Geology 104:1111-1141.

Maydagán L, Franchini M, Lentz D, Pons J, McFarlane C (2013) Sulfide composition and isotopic signature of the Altar Cu-Au deposit, Argentina: Constraints on the evolution of the porphyry-epithermal system. The Canadian Mineralogist 51:813-840.

Migdisov AA, Zezin D, Williams-Jones AE (2011) An experimental study of Cobalt (II) complexation in Cl− and H2S-bearing hydrothermal solutions. Geochimica et Cosmochimica Acta 75:4065-4079.

Naglik B, Sosnal A, Dumańska-Słowik M, Toboła T, Dimitrova D, Habryn R, Derkowski P, Czupyt Z, Woszczyna M, Markowiak M (2025) Constraints on ore vectoring from geochemical fingerprints of porphyry style pyrite. Scientific Reports 15:18696.

Nestmeyer M, Keith M, Haase KM, Klemd R, Voudouris P, Schwarz-Schampera U, Strauss H, Kati M, Magganas A (2021) Trace element signatures in pyrite and marcasite from shallow marine island arc-related hydrothermal vents, Calypso Vents, New Zealand, and Paleochori Bay, Greece. Frontiers in Earth Science 9:641654.

Ohmoto H (1972) Systematics of sulfur and carbon isotopes in hydrothermal ore deposits. Economic Geology 67:551-578.

Ohmoto H, Rye R (1979) Geochemistry of hydrothermal ore deposits In: Barnes H (ed). 2nd edn. Wiley, New York, pp 509-567.

Prokofiev V, Baksheev I, Zorina L, Belyatsky B, Ustinov V, Krivitskaya N (2012) Tourmalinization at the Darasun goldfield, Eastern Transbaikalia: Compositional, fluid inclusion and isotopic constraints. Geoscience Frontiers 3:59-71.

Prokofiev V, Brovchenko V, Zorina L, Krasnov A, Abramova V, Bortnikov N (2023) Trace Elements in Pyrite and Its Crystallization Temperature: An Example of Gold Deposits in the Darasun Goldfield, Eastern Transbaikalia, Russia. Minerals 13:288.

Prokofiev VY, Bortnikov N, Zorina L, Kulikova Z, Matel N, Kolpakova N, Il'ina G (2000) Genetic features of the Darasun gold-sulfide deposit (Eastern Transbaikal Region). Geology of Ore Deposits 42:474-495.

Prokofiev VY, Plotinskaya OY, Zorina L, Baksheev I, Kudryavtseva O, Ishkov Yu M (2004) Minerals and formation conditions of ores of the Teremkin gold deposit (Eastern Transbaikal Region, Russia). Geology of Ore Deposits 46:332-352.

Prokofiev VY, Zorina L, Kovalenker V, Akinfiev N, Baksheev I, Krasnov A, Yurgenson G, Trubkin N (2007) Composition, formation conditions, and genesis of the Talatui gold deposit, the Eastern Transbaikal Region, Russia. Geology of Ore Deposits 49:31-68.

Prokofiev VY, Bortnikov N, Kovalenker V, Vinokurov S, Zorina L, Chernova A, Kryazhev S, Krasnov A, Gorbacheva S (2010a) The Darasun gold deposit, Eastern Transbaikal Region: chemical composition, REE patterns, and stable carbon and oxygen isotopes of carbonates from ore veins. Geology of Ore Deposits 52:81-113.

Prokofiev VY, Garofalo PS, Bortnikov NS, Kovalenker VA, Zorina LD, Grichuk DV, Selektor SL (2010b) Fluid inclusion constraints on the genesis of gold in the Darasun district (eastern Transbaikalia), Russia. Economic Geology 105:395-416.

Prokofiev VY, Selector SL (2014) Fluid inclusion evidence for barbotage and its role in gold deposition at the Darasun goldfield (eastern Transbaykalia, Russia). Central European Journal of Geosciences 6:131-138.

Prokofiev VY, Tagirov B, Brovchenko V, Reukov V, Filimonova O, Zorina L, Abramova V, Kovalchuk E, Mezhueva A, Nikolaeva IY (2022) Gold in Natural and Synthetic Pyrite: A Case of the Darasun Gold District, Eastern Transbaikal Region, Russia. Geology of Ore Deposits 64:329-349.

Reich M, Kesler SE, Utsunomiya S, Palenik CS, Chryssoulis SL, Ewing RC (2005) Solubility of gold in arsenian pyrite. Geochimica et Cosmochimica Acta 69:2781-2796.

Sakharova M, Nekrasov E (1964) Mineralogical and geochemical characteristics and conditions of localization of new types of gold-sulfide ores of the Darasun deposit. Geology of Ore Deposits 3:39-55.

Savard D, Bouchard-Boivin B, Barnes S, Garbe-Schönberg D (2018) UQAC-FeS: A new series of base metal sulfide quality control reference material for LA-ICP-MS analysis Proceedings of the 10th

International Conference on the Analysis of Geological and Environmental Materials, Sydney, Australia. pp 8-13.
Sidorova N, Volkov A, Tyukova E, Kaygorodova E, Kovalchuk E, Minervina E (2025) “Invisible” gold and other impurity elements in pyrite and arsenopyrite from the Mayskoye deposit (Chukotka). Geology of Ore Deposits 67:144-160.
Slolyarov YM (1980) New data on the zoning of the Darasun deposit. Geologia:722-726.
Soulamidis G, Stouraiti C, Voudouris P, Tsikos H, Mavrogonatos C, Soukis K, Tarantola A (2026) Geochemical and mineralogical characterization of the Granitis intrusion-related hydrothermal system, northern Greece: Implications for metal zoning and exploration. Journal of Geochemical Exploration:108235.
Sung Y-H, Brugger J, Ciobanu C, Pring A, Skinner W, Nugus M (2009) Invisible gold in arsenian pyrite and arsenopyrite from a multistage Archaean gold deposit: Sunrise Dam, Eastern Goldfields Province, Western Australia. Mineralium Deposita 44:765-791.
Sykora S, Cooke DR, Meffre S, Stephanov AS, Gardner K, Scott R, Selley D, Harris AC (2018) Evolution of pyrite trace element compositions from porphyry-style and epithermal conditions at the Lihir gold deposit: Implications for ore genesis and mineral processing. Economic Geology 113:193-208.
Syverson DD, Ono S, Shanks WC, Seyfried Jr WE (2015) Multiple sulfur isotope fractionation and mass transfer processes during pyrite precipitation and recrystallization: An experimental study at 300 and 350° C. Geochimica et Cosmochimica Acta 165:418-434.
Tardani D, Reich M, Deditius AP, Chryssoulis S, Sánchez-Alfaro P, Wrage J, Roberts MP (2017) Copper–arsenic decoupling in an active geothermal system: A link between pyrite and fluid composition. Geochimica et Cosmochimica Acta 204:179-204.
Thompson JF, Newberry RJ (2000) Gold deposits related to reduced granitic intrusions.
Timofeyevsky D (1972) Geology and mineralogy of the Darasun gold area. Nedra, Moscow 260.
Tooth B, Ciobanu CL, Green L, O’Neill B, Brugger J (2011) Bi-melt formation and gold scavenging from hydrothermal fluids: An experimental study. Geochimica et Cosmochimica Acta 75:5423-5443.
Tyukova E, Voroshin S, Prokofiev VY, Vikentyev I, Abramova V, Taskaev V, Kossova S (2025) Otechestvennoe tin deposit (Magadan region, north-east Russia): genesis and bismuth mineralization. Geology of Ore Deposits 67:569-595.
Velivetskaya TA, Ignatiev AV, Yakovenko VV, Vysotskiy SV (2019) An improved femtosecond laser-ablation fluorination method for measurements of sulfur isotopic anomalies ($\Delta^{33}S$ and $\Delta^{36}S$) in sulfides with high precision. Rapid Communications in Mass Spectrometry 33:1722-1729.
Vikent'eva OV, Prokofiev VY, Gamyanin GN, Goryachev NA, Bortnikov NS (2018) Intrusion-related gold-bismuth deposits of North-East Russia: PTX parameters and sources of hydrothermal fluids. Ore Geology Reviews 102:240-259.
Vikentyev I (2015) Invisible and microscopic gold in pyrite: Methods and new data for massive sulfide ores of the Urals. Geology of ore deposits 57:237-265.
Wang H, Lan T-G, Fan H-R, Zhao L-Y, Hu H-L, Peng H-W, Xu Y, Shu L, Dai Z-H (2024) Anomalous cobalt enrichment in pyrite from an altered mafic dike in the Linglong gold deposit, Jiaodong Peninsula, China: Mechanisms and implications. Ore Geology Reviews 170:106139.
Wilson AJ, Cooke DR, Harper BJ, Deyell CL (2007) Sulfur isotopic zonation in the Cadia district, southeastern Australia: exploration significance and implications for the genesis of alkalic porphyry gold–copper deposits. Mineralium Deposita 42:465-487.
Wu Y-F, Evans K, Li J-W, Fougerouse D, Large RR, Guagliardo P (2019) Metal remobilization and ore-fluid perturbation during episodic replacement of auriferous pyrite from an epizonal orogenic gold deposit. Geochimica et Cosmochimica Acta 245:98-117.
Xiao X, Zhou T, Hollings P, White NC, Fan Y, Zhang L, Fu B (2023) Pyrite geochemistry in a porphyry-skarn Cu (Au) system and implications for ore formation and prospecting: Perspective from Xinqiao deposit, Eastern China. American Mineralogist 108:1132-1148.
Yang H, Sun H (2023) Microfabrics, in situ trace element compositions of pyrite, and the sulfur isotope chemistry of sulfides from the Xitieshan Pb-Zn deposit, Qinghai Province, northwest China: Analysis and implications. Minerals 13:1549.
Zenkov D (1946) Mine geology of the Darasun gold–arsenium deposit. Rudnichnaya Geologiya:112-134.

Zhang J, Ding Z, Bo J, Ji P, Li T, Xin W (2024) In situ trace element and S-Pb isotope study of pyrite from the denggezhuang gold deposit in the Jiaodong Peninsula—Insights into the occurrence of gold and the source of ore-forming materials. Minerals 14:158.
Zhong R, Brugger J, Chen Y, Li W (2015) Contrasting regimes of Cu, Zn and Pb transport in ore-forming hydrothermal fluids. Chemical Geology 395:154-164.
Zorin YA, Zorina LD, Spiridonov A, Rutshtein I (2001) Geodynamic setting of gold deposits in eastern and central Trans-Baikal (Chita Region, Russia). Ore Geology Reviews 17:215-232.

Supplementary Files

This is a list of supplementary files associated with this preprint. Click to download.

- SupplementaryTables.xlsx